ACS Catalysis

pubs.acs.org/acscatalysis Research Article

Cobalt-Molybdenum Oxides for Effective Coupling of Ethane Activation and Carbon Dioxide Reduction Catalysis

Rui Yao, Jayson Pinals, Roham Dorakhan, José E. Herrera, Minhua Zhang,* Prashant Deshlahra,* and Ya-Huei Cathy Chin*

Cite This: *ACS Catal.* 2022, 12, 12227−12245 Read Online

ACCESS | Metrics & More | Article Recommendations | Supporting Information

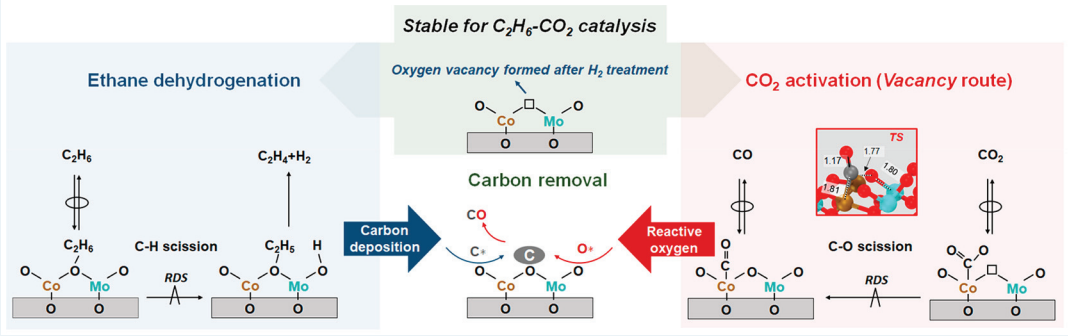

ABSTRACT: This study reports the discovery of $CoMoO_x$ moieties with synergistic catalytic roles in C_2H_6−CO_2 catalysis. C_2H_6−CO_2 catalysis occurs through multiple, concomitant catalytic cycles, initiated by the dual cycles of C_2H_6 activation and CO_2 activation, together with an undesired coke deposition cycle. C_2H_6 activation requires reactive oxygen species that assist with the kinetically relevant C−H bond activation; these oxygen species are generated from the CO_2 activation cycle within the reverse water-gas shift (RWGS) reaction. An efficient CO_2 activation in the RWGS reaction would retain higher O contents in $CoMoO_x$ moieties, leading to more effective kinetically relevant C−H bond activation of C_2H_6 and oxidation of coke precursors and thus increasing turnovers while mitigating deactivation. This mechanistic insight led us to design $CoMoO_x$ moieties, where the Co cation acts as a Lewis acid. Together with a vicinal oxygen vacancy, the Co cation activates CO_2 via a *Vacancy* route through the formation of a kinetically relevant $[Co\cdots C(O) = O\cdots \square_{vacancy}\cdots Mo]^{\ddagger}$ transition state, at which the Co interacts with the C and the oxygen vacancy ($\square_{vacancy}$) abstracts the leaving O of CO_2. The kinetically coupled cycles lead the ethane conversion rates in dehydrogenation and reforming reactions to both depend directly on the RWGS reaction rates. This mechanistic understanding of rate coupling has led to the design of $CoMoO_x$ moieties with dual functionality for effective C_2H_6−CO_2 catalysis.

KEYWORDS: *cobalt-molybdenum oxides, ethane, oxidative dehydrogenation, C−H bond activation, CO_2 activation, reverse water-gas shift, carbon deposition, deactivation*

1. INTRODUCTION

Natural gas contains predominantly light alkanes (C1−C4).[1] Its supply increase, together with its low cost, has made it an alternative feedstock for the production of commodity chemicals.[2] With up to 15 vol% ethane,[3] it is an attractive precursor for synthesizing ethylene, a versatile platform molecule for producing polyethylene, styrene, ethylene oxide, ethylene glycol, and other commodity chemicals.[4] Commercialized recently is the ethane thermal dehydrogenation process, which converts ethane to ethylene via an energetically intensive route, carried out at elevated temperatures (1023−1173 K) in order to overcome the thermodynamic constraints.[5] The thermally driven conversion is, however, unselective, because of extensive carbon losses, not only as coke deposited inside the reactor wall,[6,7] but also as other diverse carbonaceous side products (methane, propylene, acetylene, benzene, etc.). For this reason, multiple downstream separation trains, including energetically intensive compression and distillation units, are unavoidable, as they are needed for attaining high-purity ethylene from the reactor effluent.[8,9]

A more energy and atomic efficient process is the catalytic ethane conversion because it has the potential to operate at lower temperatures and produce more selective products. Scheme 1 summarizes plausible ethane reactions and the associated reaction enthalpies ($\Delta H^0_{T\,K}$) at 298 and 873 K.

Received: May 24, 2022
Revised: August 10, 2022
Published: September 26, 2022

Scheme 1. Plausible Reactions and Their Respective Reaction Enthalpy during Catalytic C_2H_6 Conversion to C_2H_4 in the Absence of an Oxidant or with CO_2, H_2O, or O_2 as the Oxidants

Reactions		$\Delta H^0_{298\,K}$ (kJ mol^{-1})	$\Delta H^0_{873\,K}$ (kJ mol^{-1})	
Ethane dehydrogenation	$C_2H_6 \rightarrow C_2H_4+H_2$	+136.5	+143.0	(Ia)
Ethane oxidative dehydrogenation (with O_2)	$C_2H_6+0.5O_2 \rightarrow C_2H_4+H_2O$	-105.4	-103.9	(Ib)
H_2 oxidation	$H_2+0.5O_2 \rightarrow H_2O$	-241.9	-247.0	(Ic)
Ethane total oxidation	$C_2H_6+3.5O_2 \rightarrow 2CO_2+3H_2O$	-1428.5	-1426.1	(IIa)
Ethane partial oxidation	$C_2H_6+2.5O_2 \rightarrow 2CO+3H_2O$	-862.5	-860.0	(IIb)
Reverse water-gas shift	$CO_2+H_2 \leftrightarrow CO+H_2O$	±41.2	±36.1	(IIIa)
Ethane oxidative dehydrogenation (with CO_2)	$C_2H_6+CO_2 \rightarrow C_2H_4+CO+H_2O$	+177.7	+179.1	(IIIb)
Ethane dry reforming	$C_2H_6+2CO_2 \rightarrow 4CO+3H_2$	+428.9	+447.0	(IVa)
Ethane steam reforming	$C_2H_6+2H_2O \rightarrow 2CO+5H_2$	+346.6	+374.9	(IVb)
Ethane hydrogenolysis	$C_2H_6+H_2 \rightarrow 2CH_4$	-65.7	-73.3	(V)
Ethane decomposition	$C_2H_6 \rightarrow 2C(graphite)+3H_2$	+84.0	+85.2	(VIa)
Boudouard reaction	$2CO \rightarrow C(graphite)+CO_2$	-172.5	-180.9	(VIb)

Without the use of an oxidant, ethane dehydrogenation (eq Ia) is an endothermic reaction ($\Delta H^0_{298\,K}$ = +136.5 kJ mol^{-1}). Several oxidation reactions, when made to occur together with ethane dehydrogenation, produce heat, thus mitigating the intensive energy requirements. One of them uses oxygen as the oxidizer—the overall reaction is called ethane oxidative dehydrogenation (ODH, eq Ib), which can be broken down into two reactions, that is, the strong endothermic dehydrogenation (eq Ia), which produces hydrogen as the co-product, coupled with the sequential, highly exothermic oxidation of the hydrogen (eq Ic; $\Delta H^0_{298\,K}$ = −241.9 kJ mol^{-1}). This reaction coupling transforms the highly endothermic, energetically intensive reaction into one that is mildly exothermic (eq Ia + Ic, which equals eq Ib; $\Delta H^0_{298\,K}$ changes from +136.5 to −105.4 kJ mol^{-1}), thus mitigating the significant external heat input required for the process. The use of O_2, however, leads to the undesired oxidation of ethane, which cleaves its C−C bond and converts it to CO_x (eqs IIa and IIb), decreasing the overall carbon atom efficiency.[10]

In contrast to O_2, CO_2 is a milder oxidant—it is a much less effective oxidizer than O_2 and therefore is called a "soft-oxidant".[5,11] Its use inhibits C_2H_6 conversion into CO and does not permit the total C_2H_6 oxidation to CO_2, thus suppressing the undesired carbon losses. Instead, CO_2 reacts with the hydrogen byproduct in the reverse water-gas shift (RWGS) reaction (eq IIIa). This reaction, when coupled together with ethane dehydrogenation, produces C_2H_4, CO, and H_2O (eq IIIb). For these reasons, CO_2 is an attractive oxidant, alternative to O_2, from the perspective of mitigating carbon losses. The use of CO_2, however, has the following drawbacks: (i) it converts a portion of the ethane to CO via the dry and steam reforming side reactions (eqs IVa and IVb) and (ii) its activation requires cleaving of its strong C═O bond, much more challenging than the activation of O_2, leading to catalyst surfaces with much lower concentrations of reactive oxygen species and oxygen chemical potentials, thus less effective oxidation of carbon debris, higher carbon chemical potentials, and in turn higher thermodynamic tendency of coke formation, compared with the use of O_2 as the oxidant.[12] An effective catalyst for C_2H_6−CO_2 reactions would require not only exceptional selectivity in taking ethane to ethylene, but also should be highly effective in activating the strong C═O bonds in CO_2, as the latter generates the reactive oxygen species required for scavenging surface carbonaceous debris, thus preventing active site losses and deactivation. There must be an optimal rate coupling of ethane and CO_2 activation cycles.

During C_2H_6−CO_2 catalysis, the identity and chemical state of catalysts influence the individual rates of the various concomitant reactions in Scheme 1 and the resulting carbon product distributions. Late transition metals (Pt,[11,13] Ni,[13] Co[13]) are known to activate ethane effectively, converting it into syngas via the undesirable hydrocarbon reforming reactions, making them unsuitable as catalysts for ethylene production. In contrast, transition metal oxides (CoO_x,[14,15] Ga_2O_3,[16] Cr_2O_3[17]) exhibit favorable selectivity to ethylene. These oxides, however, deactivate rather rapidly because of severe carbon deposition, especially during catalysis at low oxygen chemical potentials typically encountered in ethane dehydrogenation or in C_2H_6−CO_2 reactions.[13,16,18]

Herein, we embark to explore the active site requirements to realize the rate coupling of ethane and CO_2 activation cycles while interjecting the undesired coke deposition cycle during C_2H_6−CO_2 catalysis. We report a kinetic and catalyst design strategy for retaining effective ethane activation while mitigating the deactivation, through kinetic tuning of the catalytic cycles enabled by bi-functional $CoMoO_x$ active moieties. We report, through rate assessments of individual catalytic cycles and spectroscopic characterization, as well as computational studies, how the $CoMoO_x$ moieties invoke concomitant, kinetically coupled ethane activation and CO_2 activation cycles for selective and stable ethylene production. Co ions in $CoMoO_x$ moieties promote the CO_2 activation step through the creation of oxygen vacancy sites required for

https://doi.org/10.1021/acscatal.2c02525
ACS Catal. 2022, 12, 12227−12245

effective, kinetically relevant CO_2 activation. We illustrate that, by deciphering the elementary steps within the concomitant catalytic cycles and their relative rates, the CO_2 activation step contained within the RWGS cycle is the key kinetic descriptor for ethane turnovers and for maintaining the performance stability in C_2H_6−CO_2 reactions, as a direct mechanistic consequence arising from the kinetic couplings of RWGS, ethane activation (to ethylene and to reforming products), and carbon deposition rates. The interplay between the various catalytic cycles, through structures and their catalytic function tuning, leads to a selective and stable catalyst for ethylene production from C_2H_6−CO_2 mixture.

2. METHODS

2.1. Synthesis of Monometallic Molybdenum Oxide, Monometallic Cobalt Oxide, and Bimetallic Cobalt-Molybdenum Oxide Catalysts. Al_2O_3-supported molybdenum oxide, cobalt oxide, and cobalt-molybdenum oxide catalysts were prepared by the incipient wetness impregnation method. The Al_2O_3 particles (Sasol Germany, PURALOX TH 100/150, 0.96 $cm^3\ g^{-1}$ pore volume, 153 $m^2\ g^{-1}$ surface area, <75 μm particle diameter) were first heated in stagnant air to 1023 K at 0.083 K s^{-1} and then isothermally held for 8 h before cooling to 393 K. Monometallic catalysts with either 13.5 wt% molybdenum oxide or 10 wt% cobalt oxide (denoted as $13.5MoO_x/Al_2O_3$ or $10CoO/Al_2O_3$, respectively) were synthesized by impregnating the treated Al_2O_3 particles with an ammonium molybdate solution (1.3 M) or cobalt nitrate solution (0.48 M), prepared by dissolving $(NH_4)_6Mo_7O_{24}\cdot 4H_2O$ (Sigma-Aldrich, ACS reagent, 99.98% trace metals basis) or $Co(NO_3)_2\cdot 6H_2O$ (Sigma-Aldrich, 99.999% trace metal basis) precursor, respectively, in deionized water (>18.2 MΩ cm, 0.72 $cm^3\ (g_{Al_2O_3})^{-1}$ after the aforementioned heat treatment). Bimetallic catalysts with 1.5−10 wt% cobalt oxide and 13.5 wt% molybdenum oxide (denoted as yCoO−$13.5MoO_x/Al_2O_3$, y = 1.5−10) were synthesized using a similar procedure with a solution containing both $(NH_4)_6Mo_7O_{24}\cdot 4H_2O$ and $Co(NO_3)_2\cdot 6H_2O$ precursors at the targeted concentration (0.07−0.48 M cobalt nitrate solution, 1.3 M ammonium molybdate solution). After the impregnation, the samples were aged under ambient conditions for 12 h and then dried at 393 K for 12 h in stagnant air. Following this stage, samples were treated in flowing dry air (Linde, 99.99%, 0.33 $cm^3\ g_{cat}^{-1}\ s^{-1}$) by heating at 0.033 K s^{-1} to 873 K and holding isothermally at 873 K for 4 h, before cooling to ambient temperature.

2.2. Kinetic and Isotopic Assessments. A packed catalyst bed was prepared by pressing the catalyst powders (<75 μm) into pellets using a pellet die (Carver, 31 mm i.d.) at 130 MPa for 20 min in a hydraulic press (Specac) and then grinding and sieving the pellets to obtain agglomerates between 125 and 180 μm. These agglomerates were held on a quartz supporting frit to form a packed catalyst bed within a tubular microcatalytic plug flow reactor (quartz, 8.1 mm i.d.), equipped with a K-type thermocouple placed at the center (in both axial and radial directions) of the packed bed. Before rate measurements, the catalyst samples were pre-treated in situ under 1.67 $cm^3\ g^{-1}\ s^{-1}$ flowing Ar (Linde, 99.999%) at a ramp rate of 0.05 K s^{-1} to 873 K before exposure to reactants. Reactant mixtures were prepared by metering C_2H_6 (Linde certified standard, 20.0% C_2H_6 in Ar), CO_2 (Linde, 99.99%), and balanced Ar (Linde, 99.999%) independently with thermal mass flow controllers (Brooks, SLA5850). All transfer gas lines were heated and held at 383 K to prevent the condensation of water, a byproduct. Chemical compositions of the effluent stream (CO, H_2, CH_4, CO_2, C_2H_4, and C_2H_6) were quantified using a micro gas chromatograph (Varian CP-4900), equipped with HP-PLOT U and Mol Sieve 5A columns, connected to a thermal conductivity detector. Before entering the micro gas chromatograph, water was removed from the reactor effluent stream by a water trap packed with Drierite drying desiccants (Sigma-Aldrich, 98% $CaSO_4$ and 2% $CoCl_2$, 8 mesh). Steady-state rates were defined as the rates after steady-state reactions with 5 kPa C_2H_6−10 kPa CO_2 feed mixtures for 15 h at 873 K.

Isotopic exchange studies were carried out with H_2-D_2 (99.999% H_2, Linde; 99.995% D_2, Linde) and H_2-D_2O (99.999% H_2, Linde; 99.9 at% D in D_2O, Sigma-Aldrich) mixtures using the plug flow reactor system described above. Concentrations of isotopologues, that is, H_2, HD, D_2, H_2O, HDO, and D_2O, in the effluent stream were determined using an on-line mass spectrometer (Pfeiffer Omni Star), in which Ar was used as the internal standard.

2.3. Catalyst Characterization. Powder X-ray diffraction (XRD) patterns were recorded on a Rigaku Miniflex 600 diffractometer with Cu Kα (λ = 1.789 Å) radiation operating at 35 kV and 40 mA. A 2θ scan range from 10° to 80° with 0.02° increment and 0.5 s $step^{-1}$ scan speed was used for the analysis.

Raman spectra were collected using a custom-made Raman instrument equipped with an imaging spectrograph (SpectroPro-2500i, Acton Research Corporation) and a liquid nitrogen-cooled charge-coupled device (CCD) detector (Acton). The visible excitation at 532 nm was supplied by a diode-pumped solid-state (DPSS) laser with a power of around 2.0 mW at sample position. A spectral resolution of <0.5 cm^{-1} was achieved by using a 1200 lines mm^{-1} grating. The Raman shift was calibrated by interpolation of the Rayleigh line of a silicon wafer signal (520 cm^{-1}).

High-resolution X-ray photoelectron spectroscopy (XPS) was performed in a Thermo Scientific ESCALAB 250Xi Photoelectron Spectrometer (E. Grinstead, UK) equipped with a monochromatic Al Kα source (900 μm) and an environmental sample preparation chamber, which was maintained at 101 kPa with <1 ppm O_2. The fresh catalyst (labeled *oxidized* sample) was prepared by pelletizing catalyst powders into a self-supporting wafer (5 mm diameter) and then directly transferred into the sample preparation chamber without further treatment. The reduced or spent catalyst sample was prepared by treating the pelletized catalyst wafer (5 mm diameter) in a stainless-steel flow reactor (7 mm i.d.) equipped with two isolation valves in either (i) flowing H_2 for 2 h at 873 K (*reduced* sample) or (ii) in flowing H_2 for 2 h at 873 K and then in 5 kPa C_2H_6−10 kPa CO_2 reaction mixture for 15 h (*spent* sample). After these treatments, the treatment reactor was purged with flowing Ar for 12 h at 873 K before cooling to ambient temperature and subsequently isolated by closing off the valves at both ends of the reactor, before transferring to the sample preparation chamber. Under the controlled environment, the sample pellets were loaded onto a sample holder carousel and then transferred into the UHV compartment of the spectrometer for XPS analysis. The vacuum pressure in the analysis chamber was ~2 $\times 10^{-9}$ Torr, and the charge compensation was carried out using an e^-/Ar^+ flood gun. Spectrum deconvolution was carried out using Avantage and Origin software with all electron-binding energy (B.E.) values

https://doi.org/10.1021/acscatal.2c02525
ACS Catal. 2022, 12, 12227−12245

referred to the C 1s (adventitious carbon) peak at 284.5 eV. The spectra were analyzed using a Shirley background subtraction followed by deconvolution using mixed Gaussian-Lorentzian functions (70−30%). The error of the binding energy is estimated to be ±0.2 eV, and that of FWHMs is ±0.2 eV.

Diffuse reflectance UV−vis spectroscopy was carried out in a Praying Mantis (Harrick Scientific) DRS cell mounted onto a Shimadzu UV−vis 3600 spectrophotometer. The optical absorption data were obtained using a tungsten lamp (visible range, cut off at 360 nm) and a deuterium lamp (range 360−190 nm). The UV−vis spectra were referenced to a Spectralon standard (DRP-SPR, Harrick Scientific). The acquired diffuse reflectance spectra were converted into Kubelka−Munk functions $[F(R_\infty)]$.[19]

Temperature-programmed oxidation (TPO) measurements were carried out using the microcatalytic plug flow reactor system described above. For this purpose, 20 mg of spent catalyst was placed into the reactor. The sample was heated at 5 K min^{-1} from ambient temperature to 1023 K in 1.1 kPa O_2 at 90 cm^3 min^{-1} (5.0% O_2/He, Linde certified standard; He, Linde, 99.999%), during which all carbon deposits were converted to CO_2 ($C + O_2 \rightarrow CO_2$). The CO_2 evolution profiles were quantified using a methanator-FID setup. The methanator, which contains a Ni/Al_2O_3 catalyst, converted all the CO_2 into CH_4, which was then quantified using an FID detector. After each experiment, the FID detector was calibrated with pulses of CO_2 (~11.16 μmol), dosing into the carrier gas stream through a six-way valve (13 T-0345 V, Valco Instrument). Through an atomic carbon balance, the cumulative amount of CO_2 formed equals the amount of carbon deposited on the catalyst, assuming complete oxidation of the carbon. The carbon deposited on each catalyst is reported in terms of the C/Mo atomic ratio.

2.4. Density Functional Theory (DFT) Calculations. Periodic plane-wave DFT calculations were performed using the Vienna ab initio simulation package (VASP 5.4).[20−22] Wavefunctions of valence electrons were determined using the Perdew−Burke−Ernzerhof exchange-correlation functional[23] and plane wave basis functions included up to a 400 eV kinetic energy cut-off. The interactions of valence electrons with atom cores were described by the projector augmented wave method.[24] D3BJ empirical dispersion corrections[25] were used for calculating electronic energies and forces. All calculations were spin-polarized, and electronic energies were converged to $<1 \times 10^{-5}$ eV energy differences. The difference between the number of spin-up and spin-down electrons was set based on three unpaired electrons per Co^{2+} cation. Higher and lower differences were tested for all calculations to determine the electronic configurations with the lowest energy. Electron distributions near the Fermi level were treated using Gaussian smearing of 0.1 eV width, and energies were extrapolated to zero smearing.

The atomic positions in the cobalt molybdate surface were derived from the structure of $CoMoO_4$ used in a previous DFT study.[26,27] The bulk unit cell containing two $CoMoO_4$ units and orthogonal edges of lengths 4.62 Å × 5.64 Å × 4.90 Å was relaxed symmetrically in steps of 1%, and dimensions without the expansion or contraction were found to be most stable (SI, Figure S1). The unit cell was used to generate (001), (010), and (111) surfaces to determine their stability (details in SI, Figure S2). The (010) surface was found to be the most stable surface, which is consistent with the literature[27] and was used for subsequent calculations. This surface is represented by a slab with alternating Co and Mo oxide layers with four metal cations in each layer, leading to 8 Co, 8 Mo, and 32 O atoms in a 9.24 Å × 9.8 Å × 18.0 Å supercell (Figure 1). The first

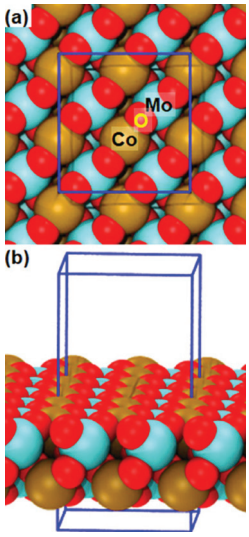

Figure 1. (a) Top view and (b) side view of the two-layer $CoMoO_4$(010) surface and the 9.24 Å × 9.8 Å × 18.0 Å supercell used in DFT calculations.

Brillouin zone for this surface was sampled using 2 × 2 × 1 Monkhorst−Pack ***k***-point meshes.[28] The convergence criterion for geometry optimizations was a maximum force of less than 0.05 V $Å^{-1}$ on any of the atoms. Dipole corrections along the [010] direction were applied to remove any long-range interactions among neighboring slabs.[29] Minimum energy paths connecting reactants, products, and surface intermediates were determined using the nudged elastic band (NEB) method.[30] Structures near the maxima in these paths were used as starting guesses to obtain transition states using the Dimer method.[31] Formation energies of all surface intermediates and transition states are referenced to bare surfaces and isolated gas-phase molecules.

Enthalpies, entropies, and Gibbs free energies were calculated using DFT-derived electronic energies and vibrational frequencies based on the formalism of ideal gas statistical mechanics, as described elsewhere[32] and in the SI (Section S3). Vibrational frequencies were calculated within harmonic approximation using 0.01 Å perturbations of atomic positions of all atoms in reactive molecular species. The imaginary frequency for each formal transition state was confirmed to be the vibration along the reaction coordinate. Low-frequency modes (below 65 cm^{-1}) were removed from vibrational partition functions and replaced by a fraction (0.7) of the partition function of gaseous CO_2 molecules because the harmonic approximation leads to significant overestimation of entropy for such low-frequency modes.

3. RESULTS AND DISCUSSION

3.1. Connections among the Rates and the Resulting Product Distributions during C_2H_6−CO_2 Catalysis on CoO−MoO_x/Al_2O_3 and Reference Monometallic $13.5MoO_x/Al_2O_3$ and $10CoO/Al_2O_3$ Catalysts. During C_2H_6−CO_2 catalysis, C_2H_4, H_2, CO, CH_4, and H_2O are formed in concomitant dehydrogenation (eq Ia, Scheme 1),

https://doi.org/10.1021/acscatal.2c02525
ACS Catal. 2022, 12, 12227−12245

Reduced

(a1)

	Carbon selectivity (%)								Formation rates (μmol s^{-1} g_{cat}^{-1})							
	$13.5MoO_x$	CoO content in CoO-$13.5MoO_x$ (wt.%)						10CoO	$13.5MoO_x$	CoO content in CoO-$13.5MoO_x$ (wt.%)						10CoO
		1.5	3	5	6.5	8	10			1.5	3	5	6.5	8	10	
C_2H_4	84.0	81.3	78.3	77.4	74.3	73.6	36.6	0	0.19	0.46	0.52	0.51	0.45	0.45	0.25	0
CO	13.3	13.7	16.6	18.4	22.1	24.0	58.7	100.0	0.03	0.08	0.11	0.12	0.14	0.15	0.39	29.25
CH_4	2.7	5.0	5.1	4.2	3.6	3.4	4.7	0	0.01	0.03	0.03	0.03	0.02	0.02	0.03	0
H_2O	-	-	-	-	-	-	-	-	0.14	0.31	0.36	0.37	0.36	0.37	0.43	37.9

(a2)

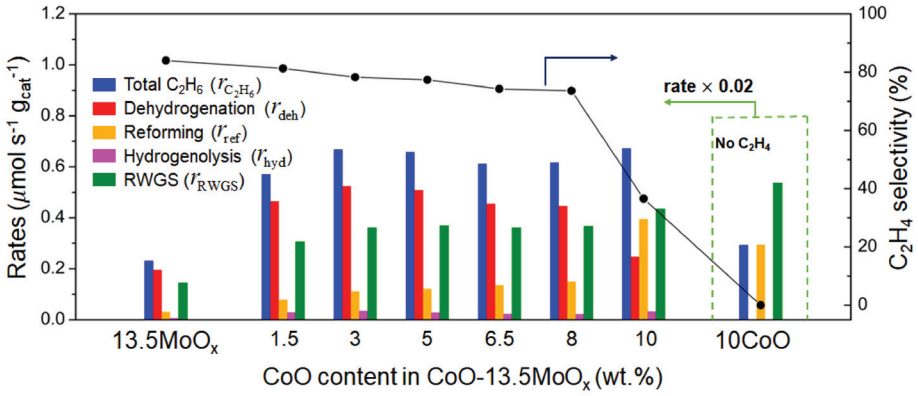

Oxidized

(b1)

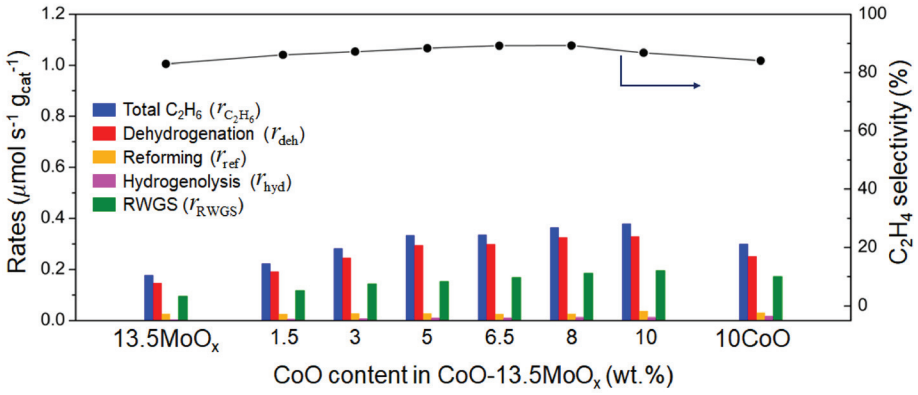

(b2)

	Carbon selectivity (%)								Formation rates (μmol s^{-1} g_{cat}^{-1})							
	$13.5MoO_x$	CoO content in CoO-$13.5MoO_x$ (wt.%)						10CoO	$13.5MoO_x$	CoO content in CoO-$13.5MoO_x$ (wt.%)						10CoO
		1.5	3	5	6.5	8	10			1.5	3	5	6.5	8	10	
C_2H_4	83.0	86.1	87.2	88.4	89.2	89.3	86.8	84.1	0.15	0.19	0.25	0.29	0.30	0.32	0.33	0.25
CO	14.7	11.3	9.8	8.3	7.5	7.2	9.9	10.3	0.03	0.03	0.03	0.03	0.03	0.03	0.04	0.03
CH_4	2.3	2.6	3.0	3.3	3.3	3.5	3.3	5.6	0	0.01	0.01	0.01	0.01	0.01	0.01	0.02
H_2O	-	-	-	-	-	-	-	-	0.10	0.12	0.14	0.15	0.17	0.18	0.20	0.17

Figure 2. Formation rates and carbon selectivities of the various products, together with the rates (per mass of catalyst) of total ethane conversion ($r_{C_2H_6}$), dehydrogenation (r_{deh}), reforming (r_{ref}), hydrogenolysis (r_{hyd}), and the concomitant rates of RWGS reaction (r_{RWGS}) on $13.5MoO_x/Al_2O_3$, $10CoO/Al_2O_3$, and a series of CoO−MoO_x/Al_2O_3 (1.5−10 wt% CoO, 13.5 wt% MoO_x) catalysts during C_2H_6−CO_2 catalysis (5 kPa C_2H_6, 10 kPa CO_2, 6000 cm^3 g_{cat}^{-1}) at 873 K and a time-on-stream of 15 h, after (a1,a2): pre-treatments in H_2 for 2 h (labeled *reduced*) or (b1,b2): pre-treatments in the inert atmosphere without a reductant (Ar for 0.5 h, labeled *oxidized*) at 873 K (for *reduced* catalyst series: C_2H_6 conversion <19% and CO_2 conversion <9%; for *oxidized* catalyst series: C_2H_6 conversion <10% and CO_2 conversion <4%).

dry or steam reforming (eqs IVa−IVb, Scheme 1), hydrogenolysis (eq V, Scheme 1), and RWGS (eq IIIa, Scheme 1) reactions. On CoO−MoO_x/Al_2O_3 catalysts (1.5−10 wt% CoO, 13.5 wt% MoO_x) and reference monometallic $13.5MoO_x/Al_2O_3$ and $10CoO/Al_2O_3$ catalysts, the rates and selectivities depended sensitively on the pre-treatment

https://doi.org/10.1021/acscatal.2c02525
ACS Catal. 2022, 12, 12227−12245

conditions of: (a) H_2 for 2 h (labeled *reduced*, upper panel) and (b) Ar for 0.5 h (unreduced, thus Co and Mo both retain their oxidized states, labeled *oxidized*, lower panel), as shown in Figure 2. These product distributions translate to steady-state catalytic rates (normalized by catalyst mass, 873 K, measured after 15 h time-on-stream) of total ethane conversion ($r_{C_2H_6}$), ethane dehydrogenation (r_{deh}), ethane reforming (r_{ref}), and ethane hydrogenolysis (r_{hyd}), together with those of the concomitant RWGS reaction (r_{RWGS}) shown in Figure 2a2,b1 for *reduced* and *oxidized* treatments, respectively. The total ethane conversion rate ($r_{C_2H_6}$) was defined as the sum of ethane dehydrogenation rate (r_{deh}), ethane reforming rate (r_{ref}), and ethane hydrogenolysis rate (r_{hyd}):

$$r_{C_2H_6} = r_{deh} + r_{ref} + r_{hyd} \quad (1)$$

The ethane dehydrogenation rate (r_{deh}) was obtained from the rate of ethylene formation; the ethane hydrogenolysis rate (r_{hyd}) was determined from the rate of methane formation, accounting for its stoichiometry, given that dry reforming is much more dominant than steam reforming (e.g., the outlet H_2O pressure of <0.6 kPa, at least an order of magnitude smaller than that of CO_2 of >9 kPa). Together with the low CO product pressures (<1.4 kPa), a product from both reforming reactions and the RWGS reaction, we can conclude that the dry reforming is the dominant reforming reaction; omitting the ethane steam reforming turnovers, the rates of ethane reforming (r_{ref}) and RWGS (r_{RWGS}, eq IIIa) reactions were calculated from the H_2 and CO formation rates, accounting for their respective reaction stoichiometries.

For *reduced* catalysts (Figure 2a1,a2), Co incorporation into MoO_x catalysts significantly increased the total C_2H_6 conversion rates and the concomitant RWGS reaction rates, per mass of catalyst, over those of the unpromoted 13.5MoO_x catalyst. Co incorporation initially increased the dehydrogenation rates, but excess Co (10 wt%) led to lower dehydrogenation rates, while the reforming rates concomitantly increased; thus selectivities toward ethylene decreased markedly from ~80±6% (1.5−8 wt% Co content) to ~37% (10 wt% Co content), as CO and H_2 became the predominant products. Despite the significant shift in the selectivity and dominant reaction pathway, ethane conversion rates ($r_{C_2H_6}$) remained essentially the same for the series of Co-promoted MoO_x catalysts at 0.57−0.67 μmol s^{-1} g_{cat}^{-1}. We have included in Table S1 of Section S4, SI, a comparison of the catalytic performance of the CoO−MoO_x/Al_2O_3 catalyst with those reported in the literature. These results suggest that, on reduced CoO−MoO_x/Al_2O_3 catalysts, the initial C−H bond activation limits the overall turnovers, but upon its activation, the sequential catalytic fate of adsorbed C_2H_5* intermediates, which traverse down the reaction coordinate and form either C_2H_4 or CO_x, depends on the Co loadings. For the contrasting case of the monometallic 10CoO catalyst (10 wt% CoO), ethane conversion rates were much higher (>20 times) than those of the CoO−MoO_x catalyst series; all of the reacted C_2H_6 was essentially converted to CO and H_2 via the reforming reactions, without forming any ethylene. This sharp decrease in ethylene selectivity on the monometallic CoO catalyst suggests that Co metal clusters, formed after the reduction, are highly effective in activating C_2H_6 but not selective toward ethylene production.

For *oxidized* catalysts (Figure 2b1,b2), Co incorporation increased all rates, and the resulting carbon selectivities to ethylene remain largely unaltered (83−90%) with side products of CO (7−11%) and CH_4 (2−4%), where the full selectivity data are shown in Table S2. Compared to their reduced counterpart (in Figure 2a1,a2), however, the rates (per mass of catalyst) were 2~3 times lower. Irrespective of the treatment conditions, all catalysts (monometallic and bimetallic) exhibited low carbon selectivities to CH_4 (<6%); thus hydrogenolysis is not a dominant reaction path.

Irrespective of the Co content, the related Co-to-Mo ratios, and their pre-treatment environment, the rates of the individual reactions ($r_{C_2H_6}$, r_{deh}, r_{ref}, r_{RWGS}) are interrelated to each other, because they are direct consequences of kinetically coupled molecular sojourns—as evidenced in Figure 3, the

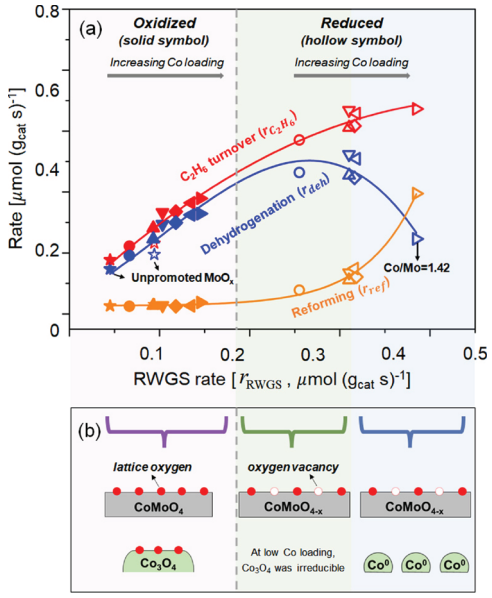

Figure 3. (a) Rates (per mass) of total C_2H_6 turnover ($r_{C_2H_6}$), dehydrogenation (r_{deh}), and reforming (r_{ref}) versus the RWGS rates (r_{RWGS}), after C_2H_6−CO_2 catalysis (5 kPa C_2H_6, 10 kPa CO_2, 6000 cm^3 g_{cat}^{-1}) for 15 h at 873 K on 13.5MoO_x (star symbol) and on a series of *y*CoO−13.5MoO_x catalysts, and (b) corresponding active phases, where for oxidized catalysts, $CoMoO_4$ and Co_3O_4 co-exist, and for reduced catalysts, $CoMoO_x$ becomes deficient of lattice oxygen, whereas any excess Co atoms not a part of the $CoMoO_x$ convert to metallic cobalt clusters. Data points are labeled according to CoO loadings, round = 1.5 wt%; up triangle = 3 wt%; down triangle = 5 wt%; diamond = 6.5 wt%; left triangle = 8 wt%; right triangle = 10 wt%. The catalysts were pre-treated in either H_2 for 2 h (*reduced*, hollow data points) or Ar for 0.5 h (*oxidized*, solid data points) before exposure to the reactant mixture.

individual rates (in *y*-axis) of ethane dehydrogenation (r_{deh}), ethane reforming (r_{ref}), and total ethane conversion ($r_{C_2H_6}$), taken from Figure 2 for the entire series of unpromoted and Co-promoted MoO_x catalysts, each shows a single correlation with the rate of RWGS reaction (r_{RWGS}, in *x*-axis) during C_2H_6−CO_2 catalysis at a constant C_2H_6 pressure (5 kPa). These rate correlations between ethane activation (r_{deh}, r_{ref}, $r_{C_2H_6}$) and CO_2 activation via the RWGS reactions (r_{RWGS}) prevail, irrespective of the pre-treatment conditions and the Co loadings, as all rate data points across the entire series of catalyst fall onto the same trendlines. These results confirm

https://doi.org/10.1021/acscatal.2c02525
ACS Catal. 2022, 12, 12227−12245

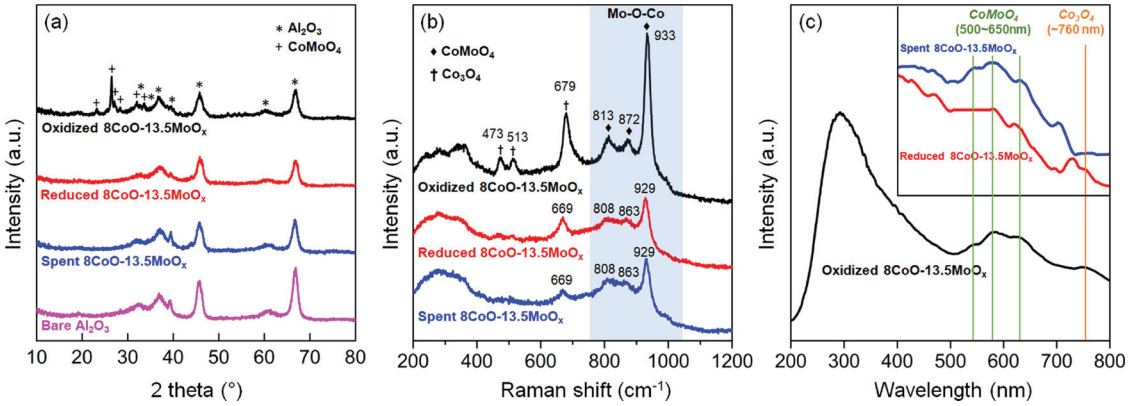

Figure 4. (a) XRD patterns, (b) Raman spectra (the bands in the shade ascribed to the Mo−O−Co stretching vibrational modes of β-$CoMoO_4$), and (c) UV−vis diffuse reflectance of *oxidized*, *reduced*, and *spent* 8CoO−13.5MoO_x catalysts (*oxidized*: pre-treated in Ar for 0.5 h at 873 K, where metal oxides retain their oxidized state; *reduced*: pre-treated in H_2 for 2 h at 873 K; *spent*: exposure of the reduced sample to 5 kPa C_2H_6−10 kPa CO_2 mixture at 873 K, 6000 $cm^3\ h^{-1}\ g_{cat}^{-1}$).

that ethane and CO_2 activation are catalytic events that are kinetically coupled together and that the rates of the RWGS reaction, which reflect the rates of CO_2 activation, dictate ethane activation and turnovers.

As shown in Figure 3, as the RWGS rates increased, the ethane dehydrogenation rates increased, whereas the reforming rates remained relatively small and increased minimally. For RWGS rates above ~0.35 μmol $g_{cat}^{-1}\ s^{-1}$, the dehydrogenation rates decreased markedly while the reforming rates increased. Among the CoO−MoO_x catalysts, the highest RWGS rate was attained at the highest Co-to-Mo atomic ratio (1.42), after reduction for 2 h at 873 K (*reduced* 10CoO−13.5MoO_x), but this rate was much lower than that of the monometallic Co catalyst (*reduced* 10CoO), as shown in Figure 2a1. The reductive treatment, when carried out on the 10CoO−13.5MoO_x catalyst, changes the electronic environment around a portion of the Co atoms and likely promotes their agglomeration into Co^0 ensembles that are not only highly effective in activating CO_2 but also in activating and cleaving the C−C bond of C_2H_6, thus promoting the undesired reforming reaction and decreasing the C_2H_4 selectivity.

Taken together, these rate correlations suggest that C_2H_6−CO_2 reactions that produce C_2H_4 occur via ethane activation on active $CoMoO_x$ moieties, where the $Co^{\delta+}$ cations promote CO_2 activation, but not active in cleaving the C−C bond of ethane. Large Co^0 ensembles, segregated from the $CoMoO_x$ moieties, activate CO_2 and promote the RWGS reaction effectively, but they are also highly effective for cleaving the C−C bond in ethane, promoting the undesired reforming pathways, which form CO and H_2. For this reason, large Co^0 ensembles formed at high Co contents on *reduced* 10CoO−13.5MoO_x or found on the monometallic 10CoO catalyst are undesired catalytic sites, because although they are effective in activating C_2H_6, they are not selective toward C_2H_4 formation.

3.2. Active Site Structures of CoO−MoO_x/Al_2O_3 and Reference Monometallic 13.5MoO_x/Al_2O_3 and 10CoO/Al_2O_3 Catalysts from Spectroscopic Characterization. Figure 4a,b shows the X-ray diffractograms and Raman spectra of the 8CoO−13.5MoO_x samples, after *oxidized* treatment and *reduced* treatment, and after exposure of a pre-reduced sample to C_2H_6−CO_2 reaction mixtures for 15 h, labeled *oxidized*, *reduced*, and *spent*, respectively. Included in Figure 4a is the XRD of the bare Al_2O_3 support. The XRD of *oxidized* 8CoO−13.5MoO_x reveals diffraction peaks attributed to β-$CoMoO_4$ crystalline (JCPDS: 21-0868), in addition to those of γ-Al_2O_3 support (JCPDS: 00-010-0425), indicating that β-$CoMoO_4$ is the dominant crystalline phase formed after the *oxidized* treatment. The presence of the β-$CoMoO_4$ phase in the *oxidized* 8CoO−13.5MoO_x sample is confirmed also with Raman spectroscopy, by the Mo−O−Co stretching vibrations observed at ~813, 872, and 933 cm^{-1} (Figure 4b)[33,34] and the three-shouldered bands present in the UV−vis diffuse reflectance spectra (Figure 4c) at 500−650 nm.[35] Raman shifts centered at 679, 473, and 513 cm^{-1} are also observed, which correspond to the A_{1g}, E_g, and F_{2g} vibrational modes of Co_3O_4,[36] respectively. Co_3O_4, however, is not detected in XRD, likely due to its small crystallite size. These results indicate the coexistence of crystalline $CoMoO_4$ and small Co_3O_4 clusters on the *oxidized* 8CoO−13.5MoO_x catalyst.

After reductive treatment (H_2 for 2 h at 873 K, *reduced* 8CoO−13.5MoO_x) and sequential C_2H_6−CO_2 catalysis for 15 h (873 K, 5 kPa C_2H_6−10 kPa CO_2, *spent* 8CoO−13.5MoO_x), the XRD diffraction patterns assigned to the $CoMoO_4$ crystalline structure disappeared and only those of the γ-Al_2O_3 support remained. As patterns associated with $CoMoO_4$ disappeared, diffraction patterns for metallic cobalt at 2θ equaling 44.35°, 51.65°, and 75.95°[37] were undetected, confirming that fully reduced cobalt species exist as small domains after reduction. Additionally, the Raman bands of β-$CoMoO_4$ and Co_3O_4 both became weaker and broader, showing a slight downshift after these two treatments—the peak at 933 cm^{-1} (β-$CoMoO_4$) shifted to 929 cm^{-1} and that at 679 cm^{-1} (Co_3O_4) shifted to 669 cm^{-1} for *reduced* and *spent* samples, respectively, which can be attributed to the generation of oxygen vacancies in the oxide lattice under H_2.[38,39]

Figure 5 shows the high-resolution Mo 3d and Co 2p XPS spectra of these samples (*oxidized*, *reduced*, and *spent* 13.5MoO_x and 8CoO−13.5MoO_x), together with the chemical state distributions of Mo 3d, obtained from peak deconvolution, and that of Co 2p, derived from assigning the spectroscopic features to Co chemical species instead of their oxidation state due to the complexity of the spectra, as previously established.[36,40] For the latter case, the satellite peak features were used to differentiate between $CoMoO_4$ and Co_3O_4 species, which are the dominant Co phases present on the *oxidized* 8CoO−13.5MoO_x catalyst, as evidenced from XRD, Raman, and UV−vis analysis, as described above.

https://doi.org/10.1021/acscatal.2c02525
ACS Catal. 2022, 12, 12227−12245

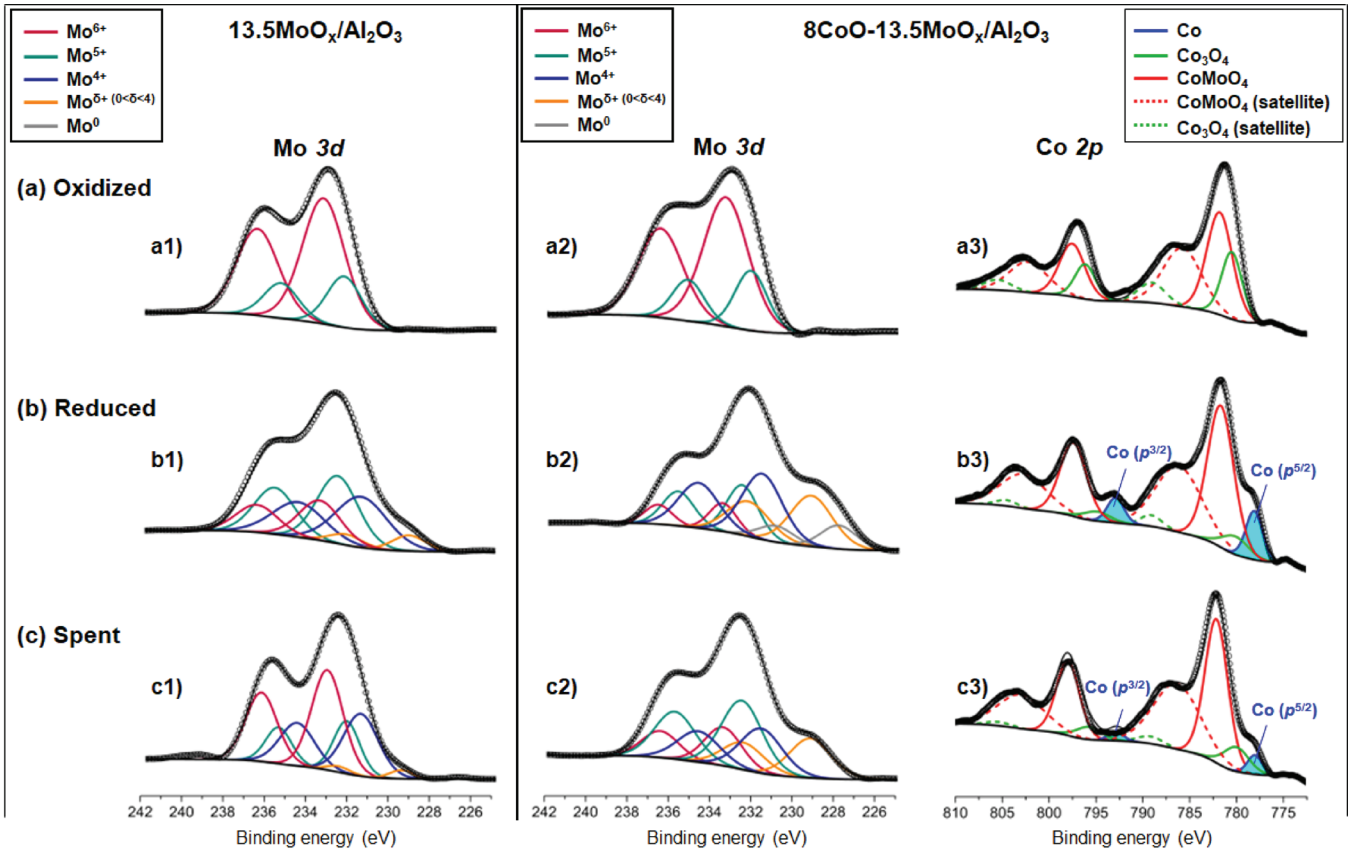

(d)

	13.5MoOx/Al2O3					8CoO-13.5MoOx/Al2O3							
	Mo distribution (atomic %)					Mo distribution (atomic %)					Co distribution (atomic %)		
	Mo^{6+}	Mo^{5+}	Mo^{4+}	$Mo^{\delta+}$	Mo^{0}	Mo^{6+}	Mo^{5+}	Mo^{4+}	$Mo^{\delta+}$	Mo^{0}	Co	Co_3O_4	$CoMoO_4$
Oxidized	75.1	24.9	-	-	-	75.5	24.5	-	-	-	0	34.3	65.7
Reduced	22.0	36.6	34.6	6.8	-	5.8	22.0	34.6	31.9	5.7	15.8	11.1	73.1
Spent	19.1	46.8	30.9	3.2	-	18.5	36.2	24.2	21.1	-	6.5	14.7	78.8

Figure 5. Mo 3d and Co 2p XPS spectra of $13.5MoO_x/Al_2O_3$ and $8CoO-13.5MoO_x/Al_2O_3$ catalysts after (a) (*oxidized*) oxidized treatment (Ar for 0.5 h), (b) (*reduced*) reduced treatment (H_2 for 2 h), and (c) (*spent*) reduction in H_2 for 2 h followed by exposure to the $C_2H_6-CO_2$ reaction mixture (5 kPa C_2H_6–10 kPa CO_2, 6000 $cm^3\ h^{-1}\ g_{cat}^{-1}$) for 15 h at 873 K, together with (d) their respective distributions of Mo chemical states and Co species.

After the *oxidized* treatment, Mo ions in both the $13.5MoO_x$ (spectrum a1) and $8CoO-13.5MoO_x$ (spectrum a2) catalysts present as a mixture of Mo^{6+} and Mo^{5+} at ~75:25 atomic ratio, with the B.E. sitting at 233.6 and 232.6 eV, respectively.[41,42] The presence of Mo^{5+} as the minority species could be attributed to the existence of strongly bound surface OH groups.[43,44] For the *oxidized* $8CoO-13.5MoO_x$ catalyst, the Co 2p region shows two features with B.E. values centered at 780.0 and 781.5 eV (spectrum a3), which can be assigned to Co_3O_4 and $CoMoO_4$ species, distributed in the sample at 34.3 and 65.7%, respectively (atomic fraction based on the Co XPS signal).[45] Taken together with the findings from XRD, Raman, and UV–vis analyses, we conclude that the dominant phases on the *oxidized* $8CoO-13.5MoO_x$ catalyst are Co_3O_4 and $CoMoO_4$ crystallites, as shown in Scheme 2a. We note that, in all spectroscopic analyses, neither the MoO_3 crystalline structure nor two-dimensional MoO_x species was detected—(i) if bulk crystalline MoO_3 exists, it would give characteristic XRD diffractions at 2θ equaling 23.7°, 25.8°, and 27.4°[46] and Raman bands at 580, 830, and 1000 cm^{-1}; we note that there is a small shoulder appeared at 1000 cm^{-1}, but it is not the main feature of the spectra, suggesting that the amount of crystalline MoO_3 is very small;[47−52] (ii) if two-dimensional MoO_x species exists, it would give the Mo=O stretching vibrational band centered at ~950 cm^{-1} in the Raman spectrum, as found in the monometallic 13.5 wt% MoO_x/Al_2O_3 catalyst (in Figure S3).

After the *reductive* treatment, the Mo^{6+} fraction in the monometallic $13.5MoO_x$ catalyst markedly decreased from 75.1 to 22.0%, where a majority of the Mo ions exists as Mo^{5+} (36.6%), Mo^{4+} (34.6%), and $Mo^{\delta+}$ (6.8%, $0 < \delta < 4$) states (*reduced* $13.5MoO_x$, spectrum b1). The same reductive treatment carried out on the $8CoO-13.5MoO_x$ catalyst (*reduced* $8CoO-13.5MoO_x$, spectrum b2) decreased the

https://doi.org/10.1021/acscatal.2c02525
ACS Catal. 2022, 12, 12227−12245

Scheme 2. Schematic Representation of Co and Mo Species Present on (a) *Oxidized*, (b) *Spent*, and (c) *Reduced* 8CoO−13.5MoO$_x$ Catalysts, Respectively; (d) Oxygen Vacancy Densities ($\square_{vacancy}$-to-Total Metal Atomic Ratio (Where Metal = Co + Mo in the Catalyst Bulk), Derived from Oxygen Chemical Titration, on 8CoO−13.5MoO$_x$ (orange rectangle) and 13.5MoO$_x$ (green rectangle) Catalysts after Treating at 873 K under (i) (Condition 1_{H_2}) in 100 kPa H_2 Treatment, (ii) (Condition $2_{CO_2+H_2}$) in 10 kPa CO_2−0.5 kPa H_2, and (iii) (Condition 3_{CO_2}) in 10 kPa CO_2

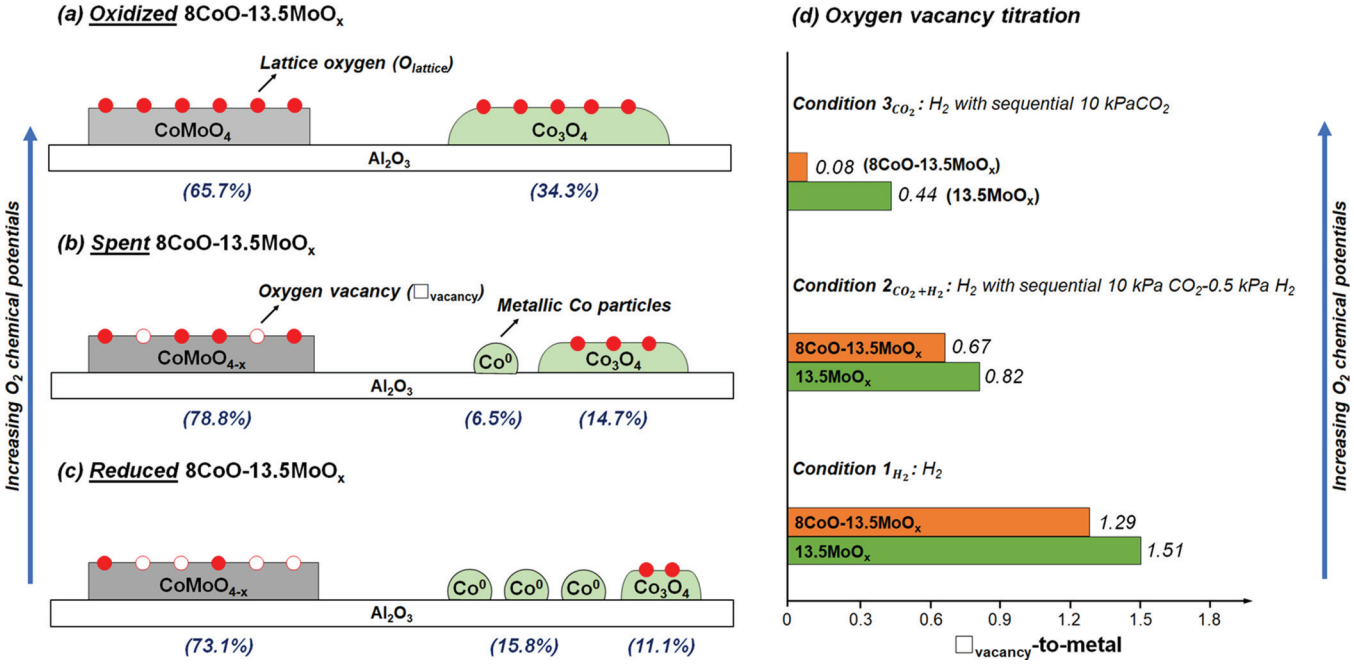

average Mo oxidation state to a larger extent, when comparing with 13.5MoO$_x$, where 94.2% Mo retained an oxidation state below +6, much higher than the 78% detected on 13.5MoO$_x$ catalyst. Notably, the catalyst contained a large fraction of highly reduced $Mo^{\delta+}$ (31.9%) species and even features with binding energies close to those attributed to highly reduced Mo (5.7%, B.E. at ∼227.8 eV), suggesting that Co incorporation enhances the reducibility of Mo. The treatment also decreased the Co_3O_4 fraction from 34.3 to 11.1% and concomitantly increased the metallic cobalt content, as evidenced by new features at ∼778.0 and ∼792.9 eV (Co $p^{3/2}$ and Co $p^{5/2}$, respectively), as shown in spectrum b3 (light blue areas). This Co_3O_4 reduction was also indicated by the downshift of the Co_3O_4 band (679 cm^{-1} for *oxidized* vs 669 cm^{-1} for *reduced* catalyst) in the Raman spectra. These changes in chemical state distribution resulted in a slight increase in the contribution of the XPS features assigned to $CoMoO_4$ species (from 65.7 to 73.1%, Figure 5d). This slight increase, however, is likely not caused by a real increase in the $CoMoO_4$ content and instead is most likely linked to the formation of CoO species from Co_3O_4 reduction.[53] These Co^{2+} species could not be differentiated from those in $CoMoO_4$ by peak deconvolution of the Co spectra because of their similar binding energies (e.g., Co $2p^{3/2}$ of 780.5−780.9 eV for CoO vs 780.9−781.3 eV for $CoMoO_4$).[54] These results suggest that, in the presence of Mo species, Co^{2+} in the $CoMoO_4$ phase remains well-dispersed, instead of over-reducing and sintering into small metallic cobalt ensembles.[55] The partial reduction of the $CoMoO_4$ phase was also evidenced by the disappearance of diffraction peaks associated with crystalline $CoMoO_4$ in the XRD patterns (Figure 4a) and the weakening and slight downshift of crystalline $CoMoO_4$ bands, which move from 933, 872, and 813 cm^{-1} to 929, 863, and 808 cm^{-1}, respectively, in the Raman spectra (Figure 4b) after the reductive treatment. In addition, the UV−vis spectrum of the reduced 8CoO−13.5MoO$_x$ catalyst shows features associated with $CoMoO_4$ (inset of Figure 4c), despite excessive scattering which affects the signal intensities, confirming that a portion of the $CoMoO_4$ moieties remains after the treatment.

Taking all these analyses together, a clear picture begins to emerge, as shown in Scheme 2c: upon reductive treatment, the dominant phases on the 8CoO−13.5MoO$_x$ catalyst are metallic cobalt ensembles and the partially reduced $CoMoO_x$ phases in which Co^{2+} species, originally from $CoMoO_4$, remain dispersed within a heavily distorted $CoMoO_4$ crystalline structure.

Exposure of the catalysts to a reaction mixture containing 5 kPa C_2H_6−10 kPa CO_2 at 6000 $cm^3\ g_{cat}^{-1}\ h^{-1}$ for 15 h at 873 K led to changes in the chemical states, as evidenced in Figure 5c1 for the 13.5MoO$_x$ catalyst and Figure 5c2,c3 for the 8CoO−13.5MoO$_x$ catalyst. During catalysis under this reaction condition, H_2 was formed (0.3∼0.7 kPa in the reactor effluent stream). The presence of a small amount of H_2, together with the CO_2 oxidant, determines the oxygen chemical potential at the catalyst surface, which, when placed on a relative scale, is much lower than that on the surface exposed to *oxidized* treatment conditions but higher than that exposed to *reductive* treatment under pure H_2. After steady-state catalysis, the Mo ions in the *spent* 13.5MoO$_x$ catalyst (spectrum c1) exist in diverse chemical states—a small fraction as Mo^{6+} (19.1%) with a majority of Mo as Mo^{5+} (46.8%) and Mo^{4+} (30.9%) cations, which translate to an average Mo chemical state of +4.8, as tabulated in Figure 5d. This distribution is similar to that after *reductive* treatment, with a marginal increase, where the average Mo state is +4.6. For the *spent* 8CoO−13.5MoO$_x$ catalyst (spectrum c2), Mo ions after catalysis are much more oxidized

https://doi.org/10.1021/acscatal.2c02525
ACS Catal. 2022, 12, 12227−12245

than its reduced counterpart—an average oxidation state of +4.3 with 18.5 Mo^{6+}: 36.2 Mo^{5+}: 24.2 Mo^{4+}: 21.1 $Mo^{\delta+}$ after reaction vs +3.4 with 5.8 Mo^{6+}: 22.0 Mo^{5+}: 34.6 Mo^{4+}: 31.9 $Mo^{\delta+}$: 5.7 Mo^0 after the reductive treatment. Notably, after reaction, XPS Mo 3d features with binding energies close to that of metallic Mo species, which were found after reduction in the *reduced* 8CoO−13.5MoO_x, were no longer detected, suggesting that, after coming in contact with the reaction mixture, these highly reduced Mo species were oxidized or carburized to oxides or carbide/oxy-carbide species.[12] In terms of the Co chemical state, the fraction of metallic cobalt in the 8CoO−13.5MoO_x decreased from 15.8% in the reduced sample to 6.5% after C_2H_6−CO_2 catalysis (spectrum c3). However, this decrease does not result in a significant surge in Co_3O_4 content. These changes in the chemical state distributions of Mo and Co indicate that both metallic cobalt and partially reduced $CoMoO_x$ phases coexist on CoO−MoO_x catalysts after the *reductive* treatment. Exposure of the catalyst to C_2H_6−CO_2 reaction mixtures led to partial oxidation of these species—CO_2 as a mild oxidant is able to partially oxidize Co^0 and $CoMoO_x$ to some extent but not far enough to re-crystallize them into Co_3O_4 and $CoMoO_4$ species, respectively, as illustrated in Scheme 2b and confirmed in both the XRD patterns and Raman spectra between the *reduced* and *spent* samples (Figure 4).

To illustrate the distinct chemical environment of Co atoms embedded in $CoMoO_x$ to that of monometallic Co metal and oxides, XPS studies were carried out on a reference monometallic 10CoO/Al_2O_3 catalyst after the *oxidized* and *reduced* treatments, as shown in Figure S4. On the *oxidized* 10CoO sample, the Co $2p^{2/3}$ features at ∼780.0 and ∼781.2 eV, which can be ascribed to Co_3O_4 and CoO (or Co aluminate) species at their Co atomic ratio of 59.0:41.0, respectively, were detected (Figure S4a). This monometallic Co reference sample that contains Co_3O_4 and CoO (or Co aluminate) exhibits much lower reactivity than the *reduced* 8CoO−13.5MoO_x/Al_2O_3 catalyst; thus irreducible Co species (Co_3O_4, CoO, or Co aluminate) are relatively inactive. In contrast, the *reduced* 10CoO sample showed a new Co $2p^{2/3}$ feature associated with metallic Co at ∼778.0 eV[45,56] that was not observed on the *oxidized* 10CoO sample. Quantitative analysis of these spectra shows that the distribution of Co among all species present in the catalyst decreases from 59.0% for Co_3O_4 in the *oxidized* 10CoO sample to 16.7% in the *reduced* 10CoO sample, while at the same time the distribution of metallic Co increases commensurately from undetectable to 27.9%. This change is much larger than that observed in the bimetallic 8CoO−13.5MoO_x catalyst (Figure 5), where only 15.8% of Co atoms are reduced. This result confirms that, without Mo, Co species are more reducible, that is, Co_3O_4 or CoO species (in the monometallic 10CoO catalyst) are more likely to be reduced to metallic Co particles than the Co embedded in the $CoMoO_4$ structures, as also reported by others.[57−59] As established, metallic Co,[13,60] together with other late transition metals (Ni,[13,60] Pt,[13,61,62] Pd,[61] Ru,[61−63] Rh[61,62]), is extremely reactive for alkane reforming reactions rather than the oxidative dehydrogenation reaction. The *reduced* 10CoO sample displayed much higher turnovers, >20 times higher than those of CoO−MoO_x series, but these C_2H_6 turnovers led exclusively to reforming products (CO and H_2) without producing any ethylene. Taken together, we conclude that metallic cobalt (Co^0) ensembles in 10CoO/Al_2O_3 and 8CoO−13.5MoO_x/Al_2O_3 catalyze the reforming reaction, as these ensembles are effective but not selective—they not only activate C_2H_6 and CO_2 but also cleave the C−C bond of C_2H_x* intermediates effectively, leading to the undesirable CO and H_2 formation.

Oxygen vacancy titration studies probe the change in the redox properties of the 8CoO−13.5MoO_x catalyst after exposure to different atmospheres (experimental details are described in SI, Section S8), listed below in the order of increasing oxygen chemical potential of: (i) condition 1_{H_2}, reduction in H_2 for 2 h at 873 K, (ii) condition $2_{CO_2+H_2}$, pre-reduction in H_2 for 2 h, followed by exposure to 10 kPa CO_2−0.5 kPa H_2 for 2 h at 873 K—this CO_2−H_2 mixture was used to mimic the effluent compositions of the C_2H_6−CO_2 reaction environment, where H_2 was generated from the dehydrogenation reaction (eq Ia), except that C_2H_6 was not present here, and (iii) condition 3_{CO_2}, pre-reduction in H_2 for 2 h, followed by exposure to 10 kPa CO_2 for 2 h at 873 K. Compared with condition $2_{CO_2+H_2}$ (with a small amount of H_2), the gaseous environment in condition 3_{CO_2} (without H_2) led to higher oxygen chemical potentials. After these treatments, the site densities of oxygen vacancies ($\square_{vacancy}$), described in terms of $\square_{vacancy}$-to-total metal atomic ratio (where metal = Co + Mo in the catalyst bulk), are shown in Scheme 2d and Table S3.

After H_2 treatment (condition 1_{H_2}), the Co-free 13.5MoO_x catalyst contained 1.51 oxygen vacancies ($\square_{vacancy}$) for each Mo. This $\square_{vacancy}$-to-Mo atomic ratio decreased to 0.82 after a sequential treatment with CO_2 and a small amount of H_2 (condition $2_{CO_2+H_2}$) and to an even lower value of 0.44 after exposure to CO_2 in the absence of H_2 (condition 3_{CO_2}). Upon exposure to atmospheres with increasing oxygen chemical potentials (from conditions 1_{H_2} < $2_{CO_2+H_2}$ < 3_{CO_2}), the decrease in the $\square_{vacancy}$-to-Mo ratio and in the related surface density of oxygen vacancy indicates that CO_2 can activate and generate reactive oxygen adatoms that refill a portion of the lattice oxygen vacancies in MoO_x domains.

For the case of the 8CoO−13.5MoO_x catalyst, the reductive treatment (condition 1_{H_2}) created vacancies at an $\square_{vacancy}$-to-total metal atomic ratio of 1.29. After the sequential CO_2−H_2 treatment (condition $2_{CO_2+H_2}$), the $\square_{vacancy}$-to-metal ratio decreased to 0.67, indicating that a portion of partially reduced Co−Mo moieties has been oxidized by CO_2 to some extent when cofeeding with a small amount of H_2. Interestingly, the $\square_{vacancy}$-to-metal ratio decreased to nearly zero (0.08) after sequential contacting to CO_2 in the absence of H_2 (condition 3_{CO_2}), confirming that Co centers in $CoMoO_4$ can activate CO_2 in order to generate the reactive oxygen species more effectively than the unpromoted 13.5MoO_x catalyst. The CO_2 activation produces oxygen adatoms, replenishing the oxygen vacancies on $CoMoO_x$ structures.

The findings from XRD, Raman, and XPS studies suggest that, on the 8CoO−13.5MoO_x catalyst (*reduced* 8CoO−13.5MoO_x), reductive treatments lead to two distinct cobalt species: metallic cobalt (Co^0) and Co^{2+} domains surrounded by MoO_x moieties (Scheme 2c). As discussed above, this catalyst exhibits very stable reactivity in C_2H_6−CO_2 catalysis, and the $CoMoO_x$ phases are responsible for selective C_2H_4 formation (∼75% selectivity). In fact, the catalyst activity is much more stable than the Co-free 13.5MoO_x catalyst after the same reductive treatment (*reduced* 13.5MoO_x catalyst, Figure

https://doi.org/10.1021/acscatal.2c02525
ACS Catal. 2022, 12, 12227−12245

Scheme 3. Catalytic Cycles and the Associated Elementary Steps of C_2H_6–CO_2 Reactions on CoO–MoO_x Catalysts, Which Include Ethane Dehydrogenation (*cycle* 1), RWGS (*cycle* 2), and Carbon Removal Event (*cycle* 3) on $CoMoO_x$ Active Moieties, Together with Ethane Reforming and RWGS on Metallic Co Ensembles (Formed only after Pre-treatment in H_2) (*Cycle* 4)[a]

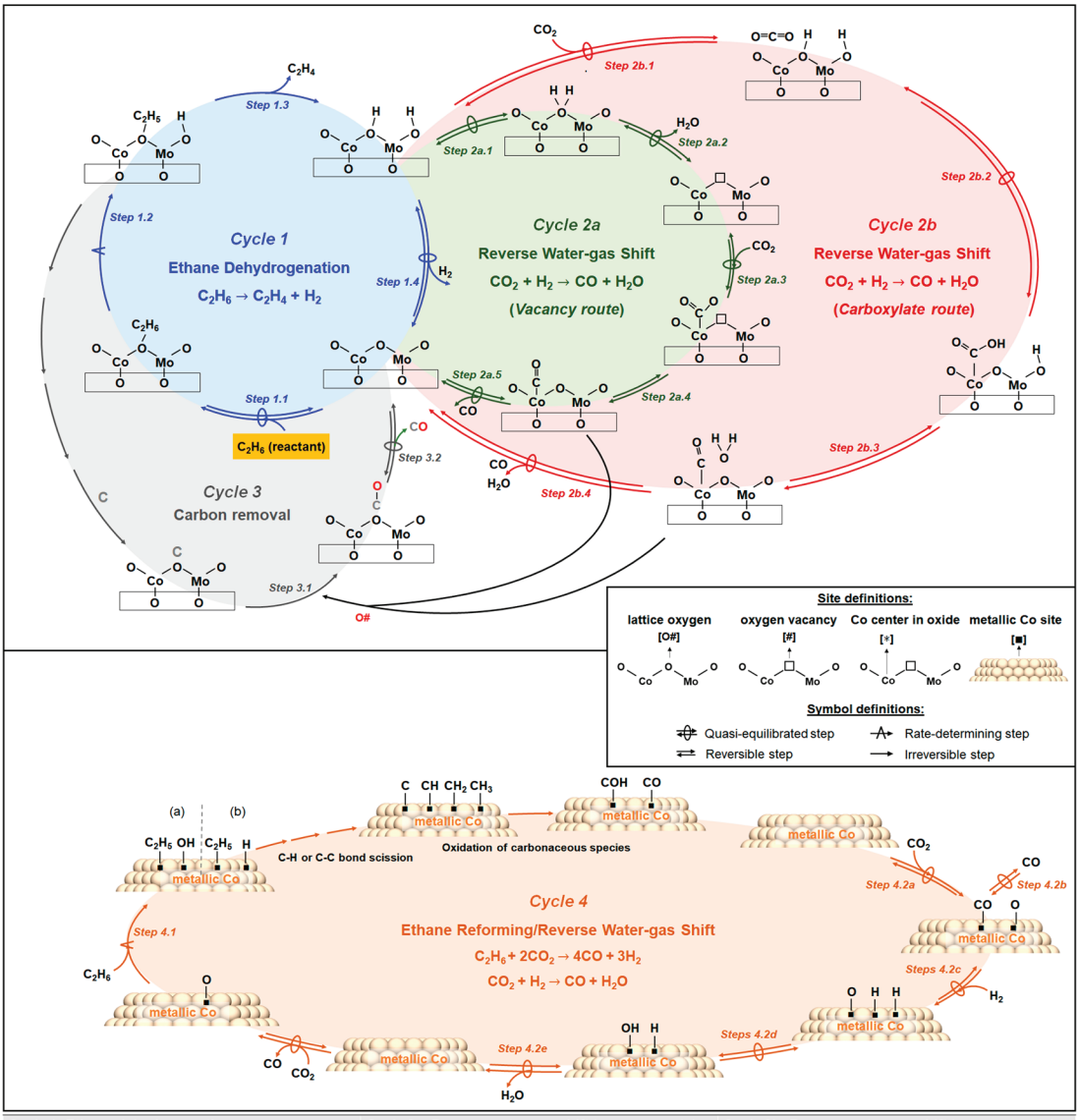

Cycle 1: Ethane dehydrogenation		**Cycle 2a: Reverse water-gas shift (vacancy route)**		**Cycle 2b: Reverse water-gas shift (vacancy route)**	
Step 1.1	$C_2H_6 + O\# \rightleftharpoons C_2H_6O\#$	Step 2a.1	$OH\# + OH\# \rightleftharpoons H_2O\# + O\#$	Step 2b.1	$CO_2 + * \rightleftharpoons CO_2*$
Step 1.2	$C_2H_6O\# + O\# \rightarrow C_2H_5O\# + OH\#$	Step 2a.2	$H_2O\# \rightleftharpoons H_2O + \#$	Step 2b.2	$CO_2* + OH\# \rightleftharpoons COOH* + O\#$
Step 1.3	$C_2H_5O\# \rightarrow C_2H_4 + OH\#$	Step 2a.3	$CO_2 + * \rightleftharpoons CO_2*$	Step 2b.3	$COOH* + OH\# \rightleftharpoons CO* + H_2O(a) + O\#$
Step 1.4	$OH\# + OH\# \rightleftharpoons H_2O + O\# + \#$	Step 2a.4	$CO_2* + \# \rightleftharpoons CO* + O\#$	Step 2b.4	$CO* + H_2O(a) \rightleftharpoons H_2O + CO + *$
		Step 2a.5	$CO* \rightleftharpoons CO + *$		
Cycle 3: Carbon removal					
Step 3.1	$C + O\# \rightarrow CO\#$	Step 3.2	$CO\# \rightleftharpoons CO + \#$		
Cycle 4: Ethane reforming					
Step 4.1	$C_2H_6 + O■ + ■ \rightarrow C_2H_5■ + OH■$ (a)	Step 4.2a	$CO_2 + ■ + ■ \rightleftharpoons CO■ + O■$		
	$C_2H_6 + ■ + ■ \rightarrow C_2H_5■ + H■$ (b)	Step 4.2b	$CO■ \rightleftharpoons CO + ■$		
	⋮	Step 4.2c	$H_2 + ■ + ■ \rightleftharpoons H■ + H■$		
	$\rightarrow CH_3■, CH_2■, CH■, C■$	Step 4.2d	$H■ + O■ \rightleftharpoons OH■ + ■$		
	$\rightarrow CHO■, CO■$	Step 4.2e	$OH■ + H■ \rightleftharpoons H_2O + ■ + ■$		

[a]The RWGS occurs via two different CO_2 activation routes of *Vacancy* route (*cycle* 2a) and *Carboxylate* route (*cycle* 2b) with their associated electronic energies (ΔE) and Gibbs free energies (ΔG, at 873 K, 1 atm) of intermediates and transition states on $CoMoO_4$(010) surfaces depicted in Figure 6. In *cycle* 4, C_2H_6 could activate on either the O■ − ■ site pair (a) or ■ − ■ site pair (b), with sequential C–H bonds and C–C bond scission to form CH_3■, CH_2■, CH■, or C■ intermediates, and oxidation of these carbonaceous intermediates to COH■ or CO■.

S5a). Metallic cobalt clusters, however, are not selective toward C_2H_4 formation and suffer from deactivation in reforming reactions.[13,64,65] This is indeed observed for the case of *reduced* 8CoO–13.5MoO_x catalyst, as shown in the time-dependent

https://doi.org/10.1021/acscatal.2c02525
ACS Catal. 2022, 12, 12227−12245

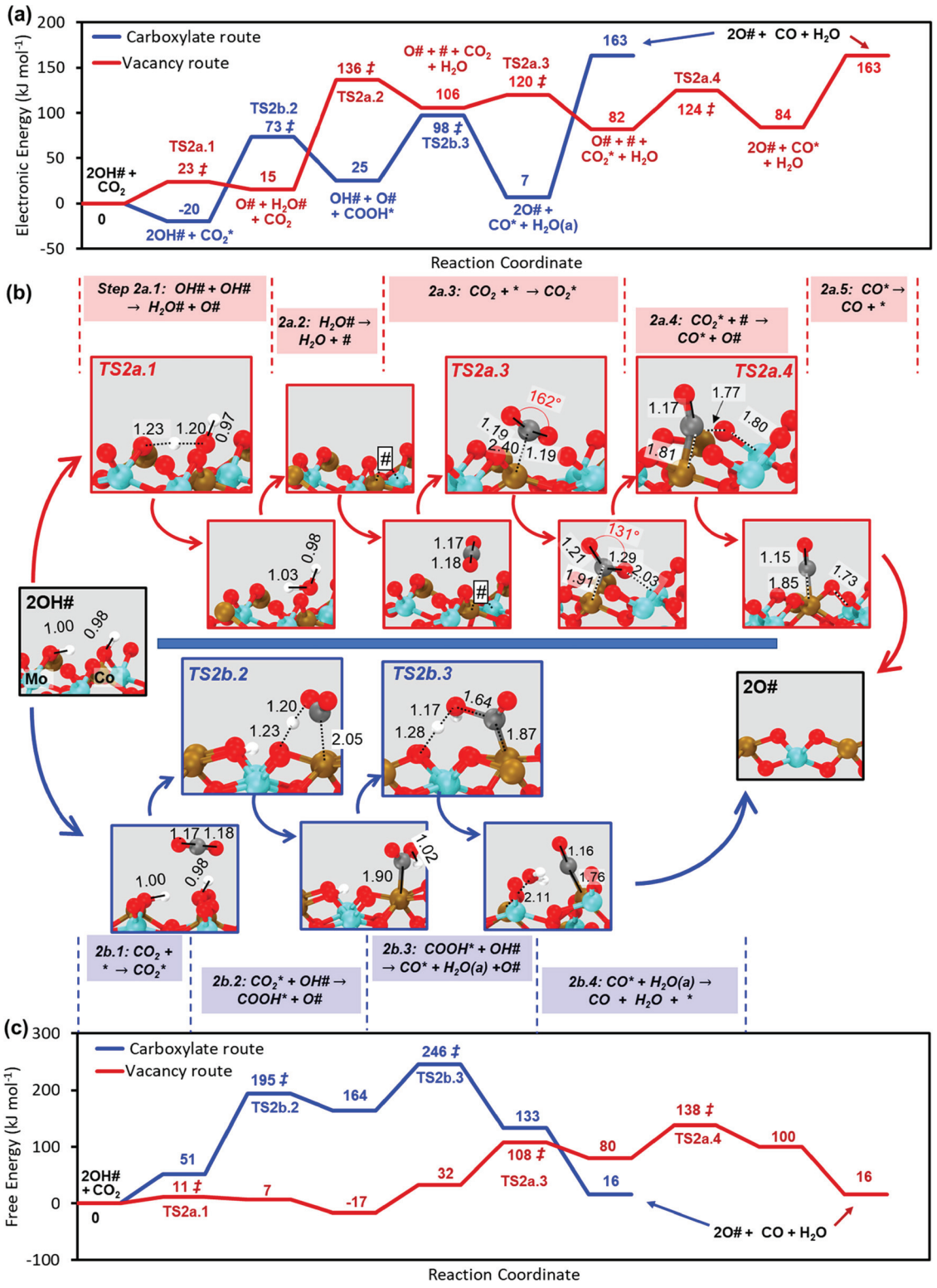

Figure 6. (a) Electronic energy (ΔE, kJ mol^{-1}) as a function of reaction coordinate, (b) elementary steps and structures of reactive intermediates and transition states, and (c) Gibbs free energy (ΔG, kJ mol^{-1}; 873 K, 1 atm) as a function of reaction coordinate, for CO_2 activation on a partially reduced $CoMoO_4$(010) surface with two H-atoms bound to lattice O-atoms in their most stable location. Bond distances in (b) are given in Å. The ΔE, ΔH, ΔS (873 K), and ΔG (873 K) values for all species relative to 2OH# and gaseous CO_2 are shown in SI (Section S12 and Table S4).

profiles of ethane dehydrogenation and reforming rates during C_2H_6−CO_2 catalysis (Figure S6)—the reforming rate decreases with time-on-stream due to the deactivation of metallic cobalt clusters, while extremely stable dehydrogenation reactivity remains. Compared to the monometallic CoO catalyst, the higher ethylene formation rate and higher ethylene selectivity observed on bimetallic CoO−MoO_x catalysts come from the $CoMoO_x$ active moieties.

Figure 3b illustrates the active site structures and their dynamics of the CoO−MoO_x catalysts. For *oxidized* CoO−

https://doi.org/10.1021/acscatal.2c02525
ACS Catal. 2022, 12, 12227−12245

MoO_x catalysts (solid symbols in Figure 3a), Co atoms mostly intercalate into molybdenum oxide domains, forming $CoMoO_4$, where the remaining Co atoms exist as Co_3O_4, especially on the samples with higher Co loadings. After pre-reduction of $CoO-MoO_x/Al_2O_3$ catalysts (*reduced* series), oxygen vacancies begin to form on $CoMoO_4$; thus oxygen-deficient $CoMoO_x$ phase prevails, causing both the dehydrogenation and RWGS rates to increase (hollow symbols in Figure 3a). These oxygen-deficient $CoMoO_x$ sites exhibit exceptional stability (for example, the deactivation constant of ~0.015 vs ~0.050 h^{-1}, for *reduced* and *oxidized* $8CoO-13.5MoO_x/Al_2O_3$ catalysts, as illustrated in Section 3.4). We note that any excess Co not as a part of the $CoMoO_x$ domains is highly effective for C_2H_6 activation but unselective, as found in the reference monometallic Co catalyst ($10CoO/Al_2O_3$), which shows a C_2H_6 conversion rate of ~14.3 μmol g_{cat}^{-1} s^{-1}, about 20 times higher than those of *reduced* $CoO-MoO_x$ catalysts, with almost zero C_2H_4 selectivity.

3.3. Ethane Dehydrogenation, RWGS, and Ethane Reforming Catalytic Cycles and Their Kinetic Coupling during $C_2H_6-CO_2$ Reactions. Next, we propose, in Scheme 3, four concomitant catalytic cycles of ethane dehydrogenation (*cycle* 1), RWGS (*cycle* 2), carbon removal (*cycle* 3), and ethane reforming (*cycle* 4), during $C_2H_6-CO_2$ catalytic sojourns on $CoO-MoO_x$ catalysts. Contained within these cycles are sequences of elementary steps, catalyzed by either $CoMoO_x$ active moieties or small metallic cobalt ensembles, the latter are formed after reductive treatments. The cooperative effects of Co and Mo centers in $CoMoO_x$ domains within the kinetically coupled catalytic cycles of ethane dehydrogenation and RWGS (*cycles* 1 and 2) lead to the exceptionally stable reactivity, much higher ethylene yields, and lower carbon deposition during $C_2H_6-CO_2$ catalysis than their monometallic counterparts.

In *Ethane Dehydrogenation* cycle (*cycle* 1), ethane first adsorbs on a lattice oxygen site (denoted as O#) of MoO_x domain in a quasi-equilibrated step (Step 1.1). Next, a neighboring lattice oxygen assists with the kinetically relevant abstraction of a hydrogen from C_2H_6 (Step 1.2), as shown previously on VO_x and MoVTeNbO catalysts during $C_2H_6-O_2$ catalysis,[66,67] via the formation of a late transition state with a nearly fully formed hydroxyl group and an adsorbed ethane derived intermediate (C_2H_5O#).[68] This intermediate could undergo a secondary, kinetically irrelevant C−H bond cleavage, forming the desired C_2H_4 (Step 1.3). Alternatively, it may also undergo C−C bond hydrogenolysis, leaving carbonaceous debris residing on the catalyst surface, as shown in *cycle* 4. These secondary events and the carbon deposition decrease the availability of the reactive lattice oxygen. In addition, in a reducing environment, the $CoMoO_x$ species have a low O-to-Mo ratio and are highly distorted with Mo ions in lower oxidation states of 3.4 after reduction and 4.3 after exposure to the reaction mixture, as shown from XPS in Figure 5. The low average O-to-Mo ratio translates to a stronger Mo═O binding strength and to much lower H abstraction rates (per lattice oxygen) than $CoMoO_4$ domains saturated with lattice oxygen atoms.[69] Additionally, the carbonaceous intermediates, in the absence of an effective oxidant, tend to agglomerate and deposit as coke, leading to catalyst deactivation (*cycle* 3).[70]

The carbonaceous intermediates could be removed by reactive oxygen species produced from the RWGS reaction, as depicted in the *Reverse Water-gas Shift* cycle (*cycle* 2, which contains two subcycles, 2a and 2b). The *Reverse Water-gas Shift* cycle includes elementary steps that activate the coreactant CO_2 as well as the sequential reaction of the adsorbed hydrogen, a coproduct from the *Ethane Dehydrogenation* cycle (*cycle* 1). This cycle is initiated by CO_2 activation, and the detailed elementary steps and their kinetic requirements derived from DFT, in terms of the electronic energy (ΔE) and Gibbs free energy (ΔG, at 873 K, 1 atm), are illustrated in Figure 6, on $CoMoO_4(010)$ surfaces, the most stable surface termination found here and in the literature.[27] A fully oxidized $CoMoO_4(010)$ surface can be reduced by H-abstraction from C_2H_6, which forms C_2H_4 (eq Ia) or by H_2 dissociation (reverse of step 1.4, *cycle 1*, Scheme 3) to form H-atom pairs bound to lattice oxygens (as OH# species, Figure 6). Several configurations of bound H-atom pairs were probed to locate the most stable configuration, which was then used for CO_2 activation. The most stable configuration of the H-atom pairs bound to lattice oxygens (2OH#) with a gas phase CO_2 at noninteracting distance is considered as the reference state for the energy values reported in Figure 6 and discussed below. Two different paths, namely *Vacancy* route and *Carboxylate* route (as *cycle* 2a and 2b, respectively), were found to be kinetically facile.

In the *Vacancy* route (*cycle* 2a), CO_2 activates on an oxygen vacancy site (denoted as #)—two adsorbed vicinal hydroxyl groups first combine and desorb as H_2O, generating an oxygen vacancy site (steps 2a.1 and 2a.2). Subsequently, CO_2 absorbs near this oxygen vacancy site (step 2a.3), followed by its OC═O bond cleavage, leaving an O# species and a CO* species bound to a Co^{2+} center (step 2a.4), before its desorption as CO that regenerates the active site (step 2a.5). The combination of hydroxyls to form H_2O in the first step of the *Vacancy* route is mediated by an O−H activation transition state (TS2a.1, Figure 6; $\Delta E^{\ddagger}$ = 23 kJ mol^{-1}, $\Delta G^{\ddagger}$ = 11 kJ mol^{-1}). Its low barrier suggests that H_2O dissociation at vacancies and the combination of hydroxyls step to form H_2O are rapid and equilibrated. H_2O desorption and the formation of O vacancies require high ΔE and low, negative ΔG of +136 and −17 kJ mol, respectively (Figure 6, step 2a.2), because the high ΔE value for the vacancy formation is compensated by the large entropy gain for H_2O desorption at the high temperature ($\Delta G = \Delta H - T\Delta S$). CO_2 absorbs near a vacancy (Figure 6, step 2a.3), and its chemisorption required bending of the linear O═C═O structure and interaction of the C-atom with a vicinal Co atom (TS2a.3, Figure 6) with activation enthalpy $\Delta E^{\ddagger}$ and activation free energy $\Delta G^{\ddagger}$ of 120 and 108 kJ mol^{-1}, respectively. The chemisorbed CO_2* species exhibits ΔE and ΔG values of 82 and 80 kJ mol^{-1}, respectively. We note that the configuration with C-atoms of CO_2 bound to Co cations was found to be most stable, as shown in Section S11, SI). The C═O bond cleavage for one of the O-atoms in CO_2* species occurs via a transition state with $\Delta E^{\ddagger}$ and $\Delta G^{\ddagger}$ values of 124 and 138 kJ mol^{-1}, respectively. The cleaved O atom replenishes the oxygen vacancy, and the resulting CO molecule is bound to the Co atom (Figure 6, step 2a.4, CO*, ΔE = 84 kJ mol^{-1}, ΔG = 100 kJ mol^{-1}). The desorption of the CO molecule leads to a fully oxidized $CoMoO_4$ surface with ΔE and ΔG of 163 and 16 kJ mol^{-1}, respectively. The CO_2 activation transition state (TS2a.4) exhibits the highest free energy along the reaction coordinate, and therefore, is kinetically relevant.

In the *Carboxylate* route (*cycle* 2b, Scheme 3), CO_2 first weakly adsorbs on the $CoMoO_4$ surface with H-atom pairs

https://doi.org/10.1021/acscatal.2c02525
ACS Catal. 2022, 12, 12227−12245

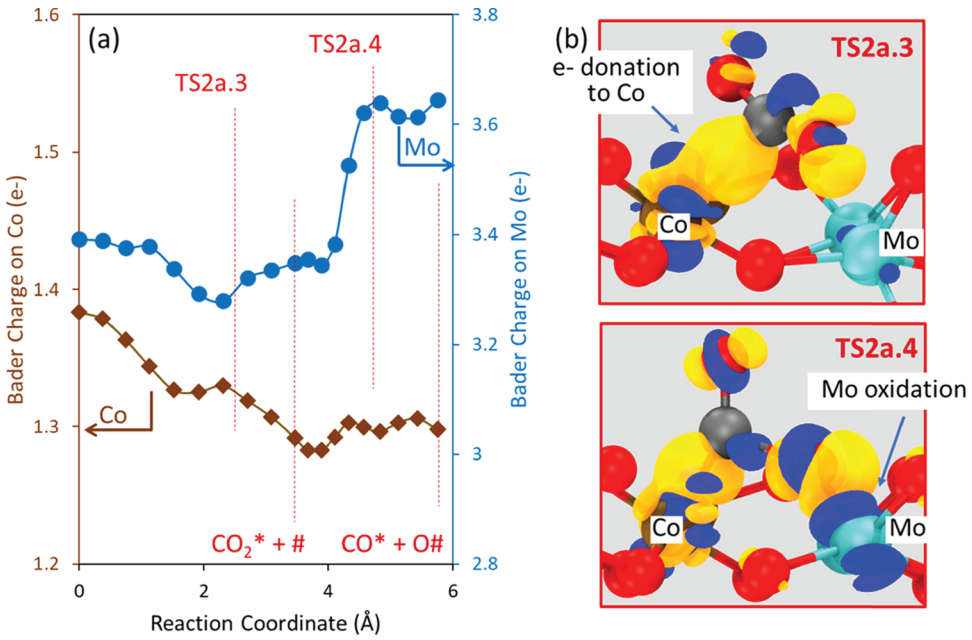

Figure 7. (a) Bader charge on Co and Mo atoms vicinal to an O vacancy (#) in a $CoMoO_x$ moieties as a function of reaction coordinate for CO_2 adsorption and OC═O bond activation at #. Lower charges reflect more electrons. Corresponding energies as a function of reaction coordinate are shown in the SI (Figure S9). (b) Isosurfaces showing the charge density difference between the optimized transition state and separate single-point calculations for neutral CO_2 and surface slab (with atomic positions fixed to that of the transition states). Orange and blue surfaces show electron accumulation and depletion, respectively. The isosurfaces are shown at charge densities 0.03 and 0.08 e $Å^{-3}$, respectively, for TS2a.3 and TS2a.4.

bound to lattice oxygens (2OH# + CO_2*, step 2b.1), which reacts with an H atom forming a COOH intermediate absorbed at a Co site (COOH*, step 2b.2). H attacks on the C- and O-atoms of CO_2 were considered, and the latter route leading to carboxylate species (instead of formate) was found to be more facile. The activation enthalpy $\Delta E^{‡}$ and activation free energy $\Delta G^{‡}$ of this transition state [Co···COO···H···O]‡ (TS2b.2) are 73 kJ mol^{-1} and 195 kJ mol^{-1}, respectively. A second H attack initiated by the H from a vicinal OH group to the COOH* species decomposes it into CO* and weakly absorbed H_2O (H_2O(a)) via a [Co···COOH···H···O]‡ (Figure 6, TS2b.3) with an activation enthalpy $\Delta E^{‡}$ and activation free energy $\Delta G^{‡}$ of 98 kJ mol^{-1} and 246 kJ mol^{-1}, respectively. The sequential desorption of CO* and H_2O(a) (steps 2b.4) leads to a fully oxidized $CoMoO_4$ surface with ΔE and ΔG values of 163 and 16 kJ mol^{-1}, respectively. In this route, the highest free energy along the reaction coordinate was found to be the transition state of the second H attack [Co···COOH···H···O]‡ (TS2b.3), making this step kinetically relevant.

The *Carboxylate* and *Vacancy* routes are analogous to the outer- and inner-sphere routes, respectively, identified for re-oxidation of OH pairs on Mo-based oxide clusters by O_2 with relative preferences that depend on temperature and H_2O pressure.[71] Here, the *Carboxylate* route exhibits lower electronic energy barriers than the *Vacancy* route (Figure 6b, $\Delta E_{TS2b.3}^{‡}$ = 98 kJ mol^{-1} vs $\Delta E_{TS2a.4}^{‡}$ = 124 kJ mol^{-1}). However, the release of H_2O prior to CO_2 activation in the *Vacancy* route leads to significant entropy gain and much lower activation free energy (Figure 6c, $\Delta G_{TS2a.4}^{‡}$ = 138 kJ mol^{-1} vs $\Delta G_{TS2b.3}^{‡}$ = 246 kJ mol^{-1} at 873 K and 1 atm H_2O). The entropy contribution to free energy would be smaller at lower temperatures, making the carboxylate route potentially more facile. However, given the large free energy difference at 873 K (138 vs. 246 kJ mol^{-1}), the vacancy route remains more facile at all practical temperatures relevant to C_2H_6–CO_2 reactions.

Co metal centers (cations) on $CoMoO_4$(010) surfaces are involved in the activation of CO_2 in both the *Carboxylate* and *Vacancy* routes (TS2a.3, TS2a.4, TS2b.2, TS2b.3; Figure 6) and the stabilization of the product CO* species (Figure 6). The alternative transition states and product states, where Mo cations instead of Co cations are the active centers, were much less stable. Furthermore, Co and Mo centers are both vicinal to the lattice O# species that accept H-atoms to dehydrogenate C_2H_6 in *Cycle 1* in Scheme 3. The catalytic roles of these metal centers are probed using Bader charge analysis shown in the SI (Section S13). The H atom pair addition partially reduces the oxide by introducing electrons into empty metal d-states.[71,72] The difference in Bader atomic charges between the surfaces with an added H atom pair and those that are uncovered and fully oxidized shows that the electrons are introduced into the Mo centers (increase by $0.25e^{-}$ and $0.3e^{-}$), while the charges on the Co centers remain essentially unchanged (Figure S8, SI). This suggests that only Mo centers are reduced by ethane of H_2 activation on stoichiometric oxide. The role of Co and Mo centers in CO_2 activation at an O vacancy is probed by Bader charges on these metals as a function of reaction coordinate and charge density differences at transition states TS2a.3 and TS2a.4, as shown in Figure 7. The charge on the Co center decreases upon the initial approach of CO_2 (TS2a.3) and remains essentially unchanged in the OC═O bond activation step (TS2a.4). The charge density difference for TS2a.3 shows that the CO_2 molecule is polarized and accumulating electron density near the Co center. This electron accumulation reflects the Lewis acid character of the Co cation. In contrast to Co, the Mo center shows a significant increase in positive charge (electron depletion) in the OC═O activation step (Figure 7b, TS2a.4) because of the oxidation of Mo by the dissociated O atom that fills the vacancy. Taken

https://doi.org/10.1021/acscatal.2c02525
ACS Catal. 2022, 12, 12227−12245

Table 1. Distribution of Dihydrogen and Water Isotopologues during H_2–D_2O Reactions (2 kPa H_2, 2 kPa D_2O, 6000 cm^3 h^{-1} g_{cat}^{-1}) at 873 K on $13.5MoO_x/Al_2O_3$ and $8CoO–13.5MoO_x/Al_2O_3$ Catalysts with Pre-treatment in H_2 for 2 h at 873 K (*Reduced*)[a,b]

	product distribution (kPa)						
	H_2	HD	D_2	H_2O	HDO	D_2O	Q/K (873 K)
$13.5MoO_x$	0.68	0.90	0.43	0.34	1.06	0.59	1.27
$8CoO–13.5MoO_x$	0.67	0.84	0.48	0.38	1.03	0.58	0.94

[a] Q denotes the reaction quotient for the H_2–D_2O reaction ($D_2 + H_2O \leftrightarrow HDO + HD$), $Q = (P_{HD}P_{HDO})/(P_{D_2}P_{H_2O})$. [b] K is the equilibrium constant for the H_2–D_2O reaction ($D_2 + H_2O \leftrightarrow HDO + HD$) at 873 K.

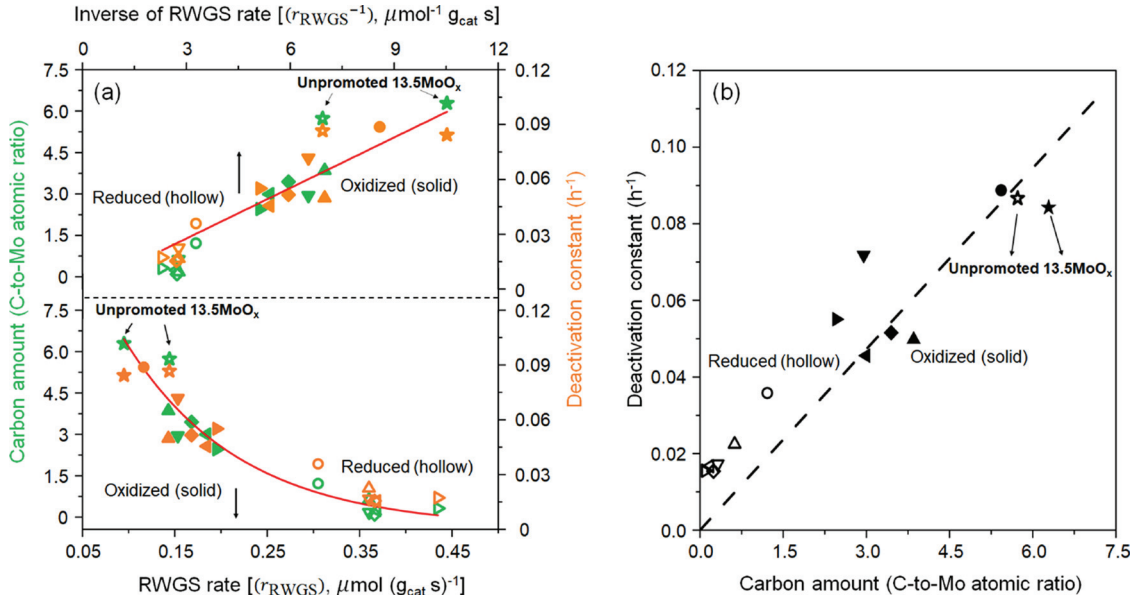

Figure 8. (a) Carbon amounts (C-to-Mo atomic ratio, green data points) derived from TPO experiments and deactivation constants (h^{-1}, eq 2, orange data points) versus the rates of RWGS reaction (r_{RWGS}) and the inverse of these rates (r_{RWGS}^{-1}), respectively, and (b) correlation between the carbon amounts after C_2H_6–CO_2 catalysis (5 kPa C_2H_6, 10 kPa CO_2, 6000 cm^3 g_{cat}^{-1}) for 15 h at 873 K and the deactivation constants derived from eq 2 on $13.5MoO_x$ (star symbols) and yCoO–$13.5MoO_x$ catalysts (y = 1.5–10, which denotes CoO loading in wt%); data points are labeled according to CoO loadings (round = 1.5 wt%; up triangle = 3 wt%; down triangle = 5 wt%; diamond = 6.5 wt%; left triangle = 8 wt%; right triangle = 10 wt%) after pre-treatments in H_2 for 2 h (*reduced*, hollow symbols) and Ar for 0.5 h (*oxidized*, solid symbols).

together, the DFT-based analyses suggest that $CoMoO_4$ oxides dehydrogenate C_2H_6 via catalytic cycles involving partial reduction of Mo centers. The re-oxidation of partially reduced $CoMoO_4$ by CO_2 is mediated by the generation on O-vacancies and facilitated by the presence of Co centers that exhibit a Lewis acid character.

We next investigate and then confirm that the activation and dissociation of CO_2, as opposed to those of H_2, the RWGS coreactant, indeed limit the RWGS rates (in *cycle* 2) and in turn dictate the rates of the concomitant C_2H_6 activation. On the reference $13.5MoO_x$ catalyst, the rates of the RWGS reaction during C_2H_6–CO_2 catalysis did not attain chemical equilibrium under all conditions reported herein—the approach-to-equilibrium value for the RWGS reaction was below 0.15 (4–16 kPa CO_2, 2–9 kPa C_2H_6, 873 K). Incorporating Co centers into the MoO_x domains, especially after the reductive pre-treatment, markedly increases the RWGS rates—the approach-to-equilibrium values significantly increased, that is, from below 0.10 to 0.37–0.55, depending on the CoO contents (1.5–10 wt%), although the chemical equilibrium was not attained. In both MoO_x and CoO–MoO_x catalyst series, the RWGS is kinetically restricted by either the dissociation of CO_2 or H_2. Isotopic exchange reactions with H_2-D_2O mixtures, carried out on both $13.5MoO_x$ and 8CoO–$13.5MoO_x$ catalysts (*reduced*) after the reductive treatments (H_2 at 873 K for 2 h), probe the reversibility of H_2 and H_2O activation within the RWGS catalytic cycle. Table 1 shows the distributions of D_2O–HDO–H_2–D_2–HD–H_2O isotopologues in the effluent stream with 2 kPa H_2–2 kPa D_2O reaction mixtures on these catalysts at 873 K at a total space velocity of 6000 cm^3 g_{cat}^{-1} h^{-1}. On both catalysts, the distributions of the D_2O–HDO–H_2–D_2–HD–H_2O isotopologues have reached the compositions expected at chemical equilibrium (0.57H_2: 0.98HD: 0.45D_2: 0.44H_2O: 0.99HDO: 0.57D_2O), with approach-to-equilibrium (Q/K) values of near unity (0.94–1.27). These isotopic distributions indicate that H_2 and H_2O activation are equilibrated and thus rule out the kinetic relevance of H_2 activation in the RWGS reaction. As a result, CO_2 dissociation must limit the RWGS rates. Activation of CO_2, which produces the reactive oxygen species, is slow on transition metal oxides, compared to that of transition metals,[73] because it requires dissociating the strong OC═O bonds. However, with the assistance of oxygen vacancies, which formed after reductive treatment, CO_2 activation became facile via the *Vacancy* route at the practical temperatures for C_2H_6 catalysis, as the DFT results indicated in Figure 6.

https://doi.org/10.1021/acscatal.2c02525
ACS Catal. 2022, 12, 12227–12245

On CoO−MoO_x catalysts, ethane reforming catalysis also occurs, but predominantly on metallic Co ensembles, as shown in the *Ethane Reforming* cycle (*cycle* 4, Scheme 3). We hypothesize that the *Ethane Reforming* cycle begins with kinetically relevant C−H bond cleavage of ethane on a cobalt-oxygen site pair (derived from CO_2 activation) resided on metallic cobalt cluster surfaces to form a C_2H_5■ and an OH■ intermediate (Step 4.1-a), as reported previously for C−H bond activation of CH_4.[60] Alternatively, the ethane activation could also occur on a Co metal atom site-pair (■ − ■) to form C_2H_5■ and H■ (Step 4.1−b). The C_2H_5■ species would undergo consecutive H abstraction, C−C cleavage, and C−O formation steps that ultimately lead to reforming products, CO and H_2; the RWGS reaction also occurs on metallic cobalt ensembles, often attaining chemical equilibriums at the conditions relevant to alkane-reforming catalysis (Steps 4.2a-e).[60]

3.4. RWGS Rates Are Kinetic Descriptors for Ethane Activation Turnovers and for Catalyst Stabilities in C_2H_6−CO_2 Reactions. The RWGS shift rates, r_{RWGS}, and the related CO_2 activation rates are key kinetic descriptors—they directly influence the ethane conversion rates in various reactions ($r_{C_2H_6}$, r_{deh}, r_{ref}), as shown in Figure 3, because the rates of CO_2 activation directly equal the rates of the generation of reactive oxygen species that prescribe the surface concentration of reactive oxygen required for scavenging the coke precursor, through the kinetic coupling of the *Reverse Water-gas Shift* cycle (*cycle* 2) and *Ethane Dehydrogenation* cycle (*cycle* 1). The coupling of the two cycles is evident in Figure 8 for the MoO_x and the series of CoO−MoO_x catalysts—the amount of surface carbon debris (expressed in terms of C-to-Mo atomic ratio) deposited on both the *reduced* and *oxidized* CoO−MoO_x catalysts, measured with TPO experiments, after C_2H_6−CO_2 reactions (5 kPa C_2H_6, 10 kPa CO_2) for 15 h at 873 K, varies inversely with the RWGS rates (r_{RWGS}, lower *x*-axis), shown as the C-to-Mo atomic ratio (green data points) versus the RWGS rates (r_{RWGS}) in Figure 8a.

Next, the extents of deactivation during C_2H_6−CO_2 reactions can be quantitatively captured, by the rate ratio of C_2H_6 conversion at time-on-stream *t*, $r_{C_2H_6,t}$, to that at the zero time ($t = 0$), $r_{C_2H_6,0}$. This rate ratio $r_{C_2H_6,t}(r_{C_2H_6,0})^{-1}$ is exponentially related to the first-order deactivation rate constant ($\alpha_{C_2H_6}$),[74,75] which reflects the time-dependent extent of rate decay during steady-state catalysis and thus is a proxy of the catalyst stability, according to:

$$\frac{r_{C_2H_6,t}}{r_{C_2H_6,0}} = \exp(-\alpha_{C_2H_6} t) \tag{2}$$

The $\alpha_{C_2H_6}$ values extracted from the time-dependent conversion profiles (Figure S5) for the series of catalysts also depended on the RWGS rates in the exact similar trends with those of the carbon content. As illustrated in Figure 8a, the first-order deactivation rate constants ($\alpha_{C_2H_6}$, orange data points) and the carbon contents (C-to-Mo atomic ratios, green data points) both decrease with increasing RWGS reactivity—indeed, both of these proxies of catalyst stability increase linearly with the inverse RWGS rates $(r_{RWGS})^{-1}$, shown in the upper *x*-axis—these direct, inverse correlations indicate that coke deposition is the key factor that causes the reactivity decay, which is further confirmed by a direct correlation between carbon amounts and deactivation constants (Figure 8b). In fact, both C-to-Mo atomic ratios (from TPO) and $\alpha_{C_2H_6}$ values depend on the RWGS similarly, (Figure 8a) that they collapse on the same profile (solid lines), albeit with different coefficients:

$$\left(\frac{C}{Mo}\right)_{C_2H_6-CO_2,873\ K,15\ h} = 0.82688\ (g_{cat}\ s\ \mu mol^{-1}) \times (r_{RWGS}\ (\mu mol\ g_{cat}^{-1}\ s^{-1}))^{-1} - 1.73666 \tag{3}$$

$$[\alpha_{C_2H_6}\ (h^{-1})]_{C_2H_6-CO_2,873\ K} = 0.01001\ (g_{cat}\ s\ \mu mol^{-1}\ h^{-1}) \times (r_{RWGS}\ (\mu mol\ g_{cat}^{-1}\ s^{-1}))^{-1} - 0.005\ (h^{-1}) \tag{4}$$

As shown in Figure 8, the spent, unpromoted MoO_x catalyst (labeled as star symbols) exhibits high C-to-Mo atomic ratios, irrespective of the pre-reduction treatment, of 6.3 for *oxidized* and 5.7 for *reduced* catalysts. The addition of Co increases the rate of the RWGS reaction and concomitantly decreases the carbon amount; notably, the reduced CoO−MoO_x series shows a much lower tendency for carbon deposition, thus exhibiting a significantly lower deactivation constant compared with its oxidized counterpart (hollow vs solid data points in Figure 8a). Taken together, we conclude that (i) Co centers polarize CO_2 and assist with its dissociation, thus generating reactive O# and increasing the RWGS rates, (ii) the increase in RWGS reactivity reduces the amount of carbon deposited during steady-state catalysis and thus mitigates rate decay due to coking, and (iii) on catalysts with Co loading exceeding the stoichiometry required for the formation of CoO−MoO_x moiety (10 wt%), large Co^0 ensembles are formed after reduction; these metallic Co^0 ensembles are not the active sites for ethylene formation, but they are highly effective for C−C bond cleavage and reforming reactions, thus causing the loss in C_2H_4 selectivity.

These findings are in agreement with those derived from XPS studies, that is, the *spent* 13.5MoO_x catalyst contains significant carbonaceous debris (C-to-Mo atomic ratio of 7.8), which explains the observed severe rate decay (Figure S5). More importantly, the *spent* 8CoO−13.5MoO_x catalyst does not contain any significant carbon debris, and its C-to-Mo atomic ratio is 0.09, which is likely the reason for their exceptional stability (Figure S5). Based on these results, it can be concluded that Co^{2+} ions intercalated into the MoO_x domains can activate CO_2 effectively, generating reactive oxygen species that are able to scavenge the carbonaceous deposits formed on $CoMoO_x$ domains, the active structures for selective ethylene formation, leading to not only high reactivity and selectivity, but also to exceptional stability for ethylene synthesis.

4. CONCLUSIONS

Catalytic ethane oxi-dehydrogenation with CO_2, a selective and "soft" oxidant, occurs under oxygen chemical potentials that are significantly lower than that with O_2 and, as a result, suffers from severe deactivation because of coke deposition. Here, we describe the intercalation of Co cations into MoO_x domains, creating $CoMoO_x$ active moieties that are highly effective for activating the CO_2, generating the reactive O

https://doi.org/10.1021/acscatal.2c02525
ACS Catal. 2022, 12, 12227−12245

species required to mitigate carbon deposition and therefore enabling stable and effective C_2H_6−CO_2 catalysis.

In terms of CO_2 activation, both *Carboxylate* and *Vacancy* routes prevail, but the high temperature relevant to C_2H_6 oxidehydrogenation catalysis favors the *Vacancy* route that involves the creation of oxygen vacancies and its subsequent catalytic role in abstracting the O of O═C═O at the kinetically relevant transition state, $[Co\cdots C(O) - O\cdots \square_{vacancy}\cdots Mo]^{\ddagger}$. In this route, Co centers (cations) on $CoMoO_x$ exhibit a Lewis acid character, interacting with the C atom of CO_2, polarizing the OC═O bond, as the vicinal oxygen vacancy abstracts one of the O of O═C═O at the transition state. The ability of Co cations in replenishing the lattice oxygen causes the Mo in $CoMoO_x$ moieties to retain a higher oxidation state and be saturated with reactive oxygen species; these reactive oxygen species then promote the C_2H_6 conversion in a parallel, kinetically coupled catalytic cycle—they assist with the kinetically relevant C−H bond activation of C_2H_6 via the formation of a late transition state, $[C_2H_5\cdots HO - Mo]^{\ddagger}$, which consists of fully formed OH and adsorbed ethane-derived fragments, as previously established.

The kinetic coupling of the dual catalytic cycles of C_2H_6 activation and CO_2 activation leads the overall C_2H_6 turnovers and the individual rates to form C_2H_4 in dehydrogenation and CO (and H_2) in reforming reactions to depend directly on the CO_2 activation rates, which are also the rates of the RWGS reaction. An effective CO_2 activation not only promotes the C_2H_6 activation but also mitigates deactivation, as it generates the reactive O* species for oxidizing the coke precursors and removing them from the catalytic sites.

In summary, deciphering the various concomitant catalytic cycles in C_2H_6−CO_2 catalysis allows us to understand the mechanistic reasons for effective C−H bond activation of C_2H_6 while minimizing coke formation. This mechanistic insight led to the design of $CoMoO_x$ moieties with synergistic functionality for effective, stable, and selective C_2H_6−CO_2 catalysis.

■ ASSOCIATED CONTENT

Supporting Information

The Supporting Information is available free of charge at https://pubs.acs.org/doi/10.1021/acscatal.2c02525.

> Effect of lattice constants on the energy of the bulk $CoMoO_4$ unit cell; stability of (001), (010), and (100) $CoMoO_4$ surfaces; enthalpy and entropy calculations; comparison of catalytic performance of the CoO−MoO_x catalyst with those of catalysts reported in the literature; carbon selectivities of products; Raman spectra of the 13.5 wt% MoO_x/Al_2O_3 catalyst; XPS analysis on the 10 wt% CoO/Al_2O_3 catalyst; oxygen vacancy titration studies; time-dependent C_2H_6 turnover rate profiles; time-dependent C_2H_6 dehydrogenation rate and reforming rate on the 8CoO−13.5MoO_x/Al_2O_3 catalyst; configuration and energies of adsorption of CO_2 on the $CoMoO_x$ surface; electronic energies, enthalpies, entropies, and free energies of intermediates and transition states; Bader charge analysis for H-addition and NEB energy profile for CO_2 activation (PDF)

■ AUTHOR INFORMATION

Corresponding Authors

Minhua Zhang − *Key Laboratory of Green Chemical Technology of Ministry of Education, R&D Center for Petrochemical Technology, Tianjin University, Tianjin 300072, China;* orcid.org/0000-0002-3426-5707; Email: mhzhang@tju.edu.cn

Prashant Deshlahra − *Department of Chemical and Biological Engineering, Tufts University, Medford, Massachusetts 02155, United States;* orcid.org/0000-0002-1063-4379; Email: Prashant.Deshlahra@tufts.edu

Ya-Huei Cathy Chin − *Department of Chemical Engineering and Applied Chemistry, University of Toronto, Toronto, Ontario M5S 3E5, Canada;* orcid.org/0000-0003-4388-0389; Phone: (416) 978-8868; Email: cathy.chin@utoronto.ca; Fax: (416) 978-8605

Authors

Rui Yao − *Department of Chemical Engineering and Applied Chemistry, University of Toronto, Toronto, Ontario M5S 3E5, Canada; Key Laboratory of Green Chemical Technology of Ministry of Education, R&D Center for Petrochemical Technology, Tianjin University, Tianjin 300072, China; Postdoctoral Programme Office, Guosen Securities Co., Ltd., Shenzhen 518001, China;* orcid.org/0000-0001-8730-9083

Jayson Pinals − *Department of Chemical and Biological Engineering, Tufts University, Medford, Massachusetts 02155, United States;* orcid.org/0000-0002-5798-7809

Roham Dorakhan − *Department of Chemical Engineering and Applied Chemistry, University of Toronto, Toronto, Ontario M5S 3E5, Canada*

José E. Herrera − *Department of Chemical and Biochemical Engineering, Western University, London, Ontario N6A 5B9, Canada;* orcid.org/0000-0003-3027-0979

Complete contact information is available at: https://pubs.acs.org/10.1021/acscatal.2c02525

Notes

The authors declare no competing financial interest.

■ ACKNOWLEDGMENTS

This study was supported by the Natural Sciences and Engineering Research Council of Canada (NSERC), Imperial Oil Limited, DCL International Inc., Canada Foundation for Innovation (CFI). We also acknowledge China Scholarship Council for a fellowship awarded to Rui Yao. J.P. and P.D. acknowledge support from US National Science Foundation (NSF award 2045675) and computational resources from eXtreme Science and Engineering Discovery Environment (XSEDE, allocation TG-CTS150005, supported by NSF award ACI-1548562).

■ REFERENCES

(1) Gomez, E.; Yan, B.; Kattel, S.; Chen, J. G. Carbon Dioxide Reduction in Tandem with Light-Alkane Dehydrogenation. *Nat. Rev. Chem.* **2019**, *3*, 638−649.

(2) Ridha, T.; Li, Y.; Gençer, E.; Siirola, J. J.; Miller, T. J.; Ribeiro, H. F.; Agrawal, R. Valorization of Shale Gas Condensate to Liquid Hydrocarbons through Catalytic Dehydrogenation and Oligomerization. *Processes* **2018**, *6*, 139.

(3) Bullin, K. A.; Krouskop, P. Compositional Variety Complicates Processing Plans for Us Shale Gas. *Oil Gas J.* **2009**, *107*, 50−55.

(4) Gärtner, C. A.; van Veen, A. C.; Lercher, J. A. Oxidative Dehydrogenation of Ethane: Common Principles and Mechanistic Aspects. *ChemCatChem* **2013**, *5*, 3196−3217.
(5) Yao, S.; Yan, B.; Jiang, Z.; Liu, Z.; Wu, Q.; Lee, J. H.; Chen, J. G. Combining CO_2 Reduction with Ethane Oxidative Dehydrogenation by Oxygen-Modification of Molybdenum Carbide. *ACS Catal.* **2018**, *8*, 5374−5381.
(6) Ren, T.; Patel, M.; Blok, K. Olefins from Conventional and Heavy Feedstocks: Energy Use in Steam Cracking and Alternative Processes. *Energy* **2006**, *31*, 425−451.
(7) Ding, D.; Zhang, Y.; Wu, W.; Chen, D.; Liu, M.; He, T. A Novel Low-Thermal-Budget Approach for the Co-Production of Ethylene and Hydrogen Via the Electrochemical Non-Oxidative Deprotonation of Ethane. *Energy Environ. Sci.* **2018**, *11*, 1710−1716.
(8) Glasier, G. F.; Pacey, P. D. Formation of Pyrolytic Carbon During the Pyrolysis of Ethane at High Conversions. *Carbon* **2001**, *39*, 15−23.
(9) Amedi, H. R.; Aghajani, M. Economic Estimation of Various Membranes and Distillation for Propylene and Propane Separation. *Ind. Eng. Chem. Res.* **2018**, *57*, 4366−4376.
(10) Carrero, C. A.; Schloegl, R.; Wachs, I. E.; Schomaecker, R. Critical Literature Review of the Kinetics for the Oxidative Dehydrogenation of Propane over Well-Defined Supported Vanadium Oxide Catalysts. *ACS Catal.* **2014**, *4*, 3357−3380.
(11) Porosoff, M. D.; Myint, M. N. Z.; Kattel, S.; Xie, Z.; Gomez, E.; Liu, P.; Chen, J. G. Identifying Different Types of Catalysts for CO_2 Reduction by Ethane through Dry Reforming and Oxidative Dehydrogenation. *Angew. Chem., Int. Ed.* **2015**, *54*, 15501−15505.
(12) Yao, R.; Herrera, J. E.; Chen, L.; Chin, Y.-H. C. Generalized Mechanistic Framework for Ethane Dehydrogenation and Oxidative Dehydrogenation on Molybdenum Oxide Catalysts. *ACS Catal.* **2020**, 6952−6968.
(13) Myint, M.; Yan, B.; Wan, J.; Zhao, S.; Chen, J. G. Reforming and Oxidative Dehydrogenation of Ethane with CO_2 as a Soft Oxidant over Bimetallic Catalysts. *J. Catal.* **2016**, *343*, 168−177.
(14) Koirala, R.; Safonova, O. V.; Pratsinis, S. E.; Baiker, A. Effect of Cobalt Loading on Structure and Catalytic Behavior of CoO_x/SiO_2 in CO_2-Assisted Dehydrogenation of Ethane. *Appl. Catal., A* **2018**, *552*, 77−85.
(15) Koirala, R.; Buechel, R.; Pratsinis, S. E.; Baiker, A. Silica Is Preferred over Various Single and Mixed Oxides as Support for CO_2-Assisted Cobalt-Catalyzed Oxidative Dehydrogenation of Ethane. *Appl. Catal., A* **2016**, *527*, 96−108.
(16) Koirala, R.; Buechel, R.; Krumeich, F.; Pratsinis, S. E.; Baiker, A. Oxidative Dehydrogenation of Ethane with CO_2 over Flame-Made Ga-Loaded TiO_2. *ACS Catal.* **2015**, *5*, 690−702.
(17) Mimura, N.; Okamoto, M.; Yamashita, H.; Oyama, S. T.; Murata, K. Oxidative Dehydrogenation of Ethane over Cr/ZSM-5 Catalysts Using CO_2 as an Oxidant. *J. Phys. Chem. B* **2006**, *110*, 21764−21770.
(18) Najari, S.; Saeidi, S.; Concepcion, P.; Dionysiou, D. D.; Bhargava, S. K.; Lee, A. F.; Wilson, K. Oxidative Dehydrogenation of Ethane: Catalytic and Mechanistic Aspects and Future Trends. *Chem. Soc. Rev.* **2021**, *50*, 4564−4605.
(19) Nobbs, J. H. Kubelka—Munk Theory and the Prediction of Reflectance. *Rev. Prog. Color. Relat. Top.* **1985**, *15*, 66−75.
(20) Kresse, G.; Furthmüller, J. Efficient Iterative Schemes for Ab Initio Total-Energy Calculations Using a Plane-Wave Basis Set. *Phys. Rev. B* **1996**, *54*, 11169−11186.
(21) Kresse, G.; Furthmüller, J. Efficiency of Ab-Initio Total Energy Calculations for Metals and Semiconductors Using a Plane-Wave Basis Set. *Comput. Mater. Sci.* **1996**, *6*, 15−50.
(22) Kresse, G.; Hafner, J. Ab Initio Molecular Dynamics for Liquid Metals. *Phys. Rev. B* **1993**, *47*, 558−561.
(23) Perdew, J. P.; Burke, K.; Ernzerhof, M. Generalized Gradient Approximation Made Simple. *Phys. Rev. Lett.* **1996**, *77*, 3865−3868.
(24) Kresse, G.; Joubert, D. From Ultrasoft Pseudopotentials to the Projector Augmented-Wave Method. *Phys. Rev. B* **1999**, *59*, 1758−1775.
(25) Grimme, S.; Ehrlich, S.; Goerigk, L. Effect of the Damping Function in Dispersion Corrected Density Functional Theory. *J. Comput. Chem.* **2011**, *32*, 1456−1465.
(26) Livage, C.; Hynaux, A.; Marrot, J.; Nogues, M.; Férey, G. Solution Process for the Synthesis of the "High-Pressure" Phase $CoMoO_4$ and X-Ray Single Crystal Resolution. *J. Mater. Chem.* **2002**, *12*, 1423−1425.
(27) Altarawneh, I. S.; Rawadieh, S. E.; Batiha, M. A.; Al-Makhadmeh, L. A.; Al-Shaweesh, M. A.; Altarawneh, M. K. Structures and Thermodynamic Stability of Cobalt Molybdenum Oxide ($CoMoO_4$-II). *Surf. Sci.* **2018**, *677*, 52−59.
(28) Monkhorst, H. J.; Pack, J. D. Special Points for Brillouin-Zone Integrations. *Phys. Rev. B* **1976**, *13*, 5188−5192.
(29) Makov, G.; Payne, M. Periodic Boundary Conditions in Ab Initio Calculations. *Phys. Rev. B* **1995**, *51*, 4014−4022.
(30) Henkelman, G.; Uberuaga, B. P.; Jónsson, H. A Climbing Image Nudged Elastic Band Method for Finding Saddle Points and Minimum Energy Paths. *J. Chem. Phys.* **2000**, *113*, 9901−9904.
(31) Henkelman, G.; Jónsson, H. A Dimer Method for Finding Saddle Points on High Dimensional Potential Surfaces Using Only First Derivatives. *J. Chem. Phys.* **1999**, *111*, 7010−7022.
(32) Liu, Y.; Twombly, A.; Dang, Y.; Mirich, A.; Suib, S. L.; Deshlahra, P. Roles of Enhancement of C−H Activation and Diminution of C−O Formation within M1-Phase Pores in Propane Selective Oxidation. *ChemCatChem* **2021**, *13*, 882−899.
(33) Li, Z.; Fu, Y.; Bao, J.; Jiang, M.; Hu, T.; Liu, T.; Xie, Y. Effect of Cobalt Promoter on Co−Mo−K/C Catalysts Used for Mixed Alcohol Synthesis. *Appl. Catal., A* **2001**, *220*, 21−30.
(34) Nti, F.; Anang, D. A.; Han, J. I. Facilely Synthesized $NiMoO_4$/$CoMoO_4$ Nanorods as Electrode Material for High Performance Supercapacitor. *J. Alloys Compd.* **2018**, *742*, 342−350.
(35) Gao, Z.; Yang, H.; Cao, Y.; Wu, Q.; Kang, L.; Mao, J.; Wu, J. Complete Mineralization of a Humic Acid by $SO_4^{\cdot-}$ Generated on $CoMoO_4/gC_3N_4$ under Visible-Light Irradiation. *Nanotechnol.* **2019**, *30*, 255704.
(36) Yang, J.; Liu, H.; Martens, W. N.; Frost, R. L. Synthesis and Characterization of Cobalt Hydroxide, Cobalt Oxyhydroxide, and Cobalt Oxide Nanodiscs. *J. Phys. Chem. C* **2010**, *114*, 111−119.
(37) Barakat, N. A. M.; El-Newehy, M.; Al-Deyab, S. S.; Kim, H. Y. Cobalt/Copper-Decorated Carbon Nanofibers as Novel Non-Precious Electrocatalyst for Methanol Electrooxidation. *Nanoscale Res. Lett.* **2014**, *9*, 2.
(38) de Castro Silva, I.; Sigoli, F. A.; Mazali, I. O. Reversible Oxygen Vacancy Generation on Pure CeO_2 Nanorods Evaluated by in Situ Raman Spectroscopy. *J. Phys. Chem. C* **2017**, *121*, 12928−12935.
(39) Lee, Y.; He, G.; Akey, A. J.; Si, R.; Flytzani-Stephanopoulos, M.; Herman, I. P. Raman Analysis of Mode Softening in Nanoparticle $CeO_{2-\delta}$ and Au-$CeO_{2-\delta}$ During Co Oxidation. *J. Am. Chem. Soc.* **2011**, *133*, 12952−12955.
(40) Herrera, J. E.; Resasco, D. E. Loss of Single-Walled Carbon Nanotubes Selectivity by Disruption of the Co−Mo Interaction in the Catalyst. *J. Catal.* **2004**, *221*, 354−364.
(41) Phillips, D. C.; Sawhill, S. J.; Self, R.; Bussell, M. E. Synthesis, Characterization, and Hydrodesulfurization Properties of Silica-Supported Molybdenum Phosphide Catalysts. *J. Catal.* **2002**, *207*, 266−273.
(42) Datta, R. S.; Haque, F.; Mohiuddin, M.; Carey, B. J.; Syed, N.; Zavabeti, A.; Zhang, B.; Khan, H.; Berean, K. J.; Ou, J. Z.; Mahmood, N.; Daeneke, T.; Kalantar-zadeh, K. Highly Active Two Dimensional α-MoO_{3-x} for the Electrocatalytic Hydrogen Evolution Reaction. *J. Mater. Chem. A* **2017**, *5*, 24223−24231.
(43) Meyer, J.; Kidambi, P. R.; Bayer, B. C.; Weijtens, C.; Kuhn, A.; Centeno, A.; Pesquera, A.; Zurutuza, A.; Robertson, J.; Hofmann, S. Metal Oxide Induced Charge Transfer Doping and Band Alignment of Graphene Electrodes for Efficient Organic Light Emitting Diodes. *Sci. Rep.* **2014**, *4*, 5380.
(44) Kim, J. H.; Dash, J. K.; Kwon, J.; Hyun, C.; Kim, H.; Ji, E.; Lee, G.-H. Van Der Waals Epitaxial Growth of Single Crystal α-MoO_3

Layers on Layered Materials Growth Templates. *2D Mater.* **2019**, *6*, No. 015016.
(45) Herrera, J.; Resasco, D. Loss of Single-Walled Carbon Nanotubes Selectivity by Disruption of the Co−Mo Interaction in the Catalyst. *J. Catal.* **2004**, *221*, 354−364.
(46) Wu, D.; Shen, R.; Yang, R.; Ji, W.; Jiang, M.; Ding, W.; Peng, L. Mixed Molybdenum Oxides with Superior Performances as an Advanced Anode Material for Lithium-Ion Batteries. *Sci. Rep.* **2017**, *7*, 44697.
(47) Chen, K.; Xie, S.; Bell, A. T.; Iglesia, E. Structure and Properties of Oxidative Dehydrogenation Catalysts Based on MoO_3/Al_2O_3. *J. Catal.* **2001**, *198*, 232−242.
(48) Chakrabarti, A.; Wachs, I. E. Molecular Structure−Reactivity Relationships for Olefin Metathesis by Al_2O_3-Supported Surface Moox Sites. *ACS Catal.* **2018**, *8*, 949−959.
(49) Mestl, G.; Srinivasan, T. K. K. Raman Spectroscopy of Monolayer-Type Catalysts: Supported Molybdenum Oxides. *Catal. Rev.* **1998**, *40*, 451−570.
(50) Thielemann, J. P.; Ressler, T.; Walter, A.; Tzolova-Müller, G.; Hess, C. Structure of Molybdenum Oxide Supported on Silica SBA-15 Studied by Raman, UV−Vis and X-Ray Absorption Spectroscopy. *Appl. Catal., A* **2011**, *399*, 28−34.
(51) Tian, H.; Roberts, C. A.; Wachs, I. E. Molecular Structural Determination of Molybdena in Different Environments: Aqueous Solutions, Bulk Mixed Oxides, and Supported MoO_3 Catalysts. *J. Phys. Chem. C* **2010**, *114*, 14110−14120.
(52) Chua, Y. T.; Stair, P. C.; Wachs, I. E. A Comparison of Ultraviolet and Visible Raman Spectra of Supported Metal Oxide Catalysts. *J. Phys. Chem. B* **2001**, *105*, 8600−8606.
(53) Nyathi, T. M.; Fischer, N.; York, A. P. E.; Morgan, D. J.; Hutchings, G. J.; Gibson, E. K.; Wells, P. P.; Catlow, C. R. A.; Claeys, M. Impact of Nanoparticle−Support Interactions in Co_3O_4/Al_2O_3 Catalysts for the Preferential Oxidation of Carbon Monoxide. *ACS Catal.* **2019**, *9*, 7166−7178.
(54) Yan, X.; Tian, L.; Atkins, S.; Liu, Y.; Murowchick, J.; Chen, X. Converting $CoMoO_4$ into CoO/MoO_x for Overall Water Splitting by Hydrogenation. *ACS Sustainable Chem. Eng.* **2016**, *4*, 3743−3749.
(55) Tan, B. J.; Klabunde, K. J.; Sherwood, P. M. A. XPS Studies of Solvated Metal Atom Dispersed (SMAD) Catalysts. Evidence for Layered Cobalt-Manganese Particles on Alumina and Silica. *J. Am. Chem. Soc.* **1991**, *113*, 855−861.
(56) McIntyre, N. S.; Johnston, D. D.; Coatsworth, L. L.; Davidson, R. D.; Brown, J. R. X-Ray Photoelectron Spectroscopic Studies of Thin Film Oxides of Cobalt and Molybdenum. *Surf. Interface Anal.* **1990**, *15*, 265−272.
(57) Arnoldy, P.; Heijkant, J.; Bok, G.; Moulijn, J. A. Temperature-Programmed Sulfiding of MoO_3/Al_2O_3 Catalysts. *J. Catal.* **1985**, *92*, 35−55.
(58) Tavizón-Pozos, J. A.; Santolalla-Vargas, C. E.; Valdés-Martínez, O. U.; de los Reyes Heredia, J. A. Effect of Metal Loading in Unpromoted and Promoted $CoMo/Al_2O_3-TiO_2$ Catalysts for the Hydrodeoxygenation of Phenol. *Catalysts* **2019**, *9*, 550.
(59) Weerakkody, C.; Rathnayake, D.; He, J.; Dutta, B.; Kerns, P.; Achola, L.; Suib, S. L. Enhanced Catalytic Properties of Molybdenum Promoted Mesoporous Cobalt Oxide: Structure-Surface-Dependent Activity for Selective Synthesis of 2-Substituted Benzimidazoles. *ChemCatChem* **2019**, *11*, 528−537.
(60) Tu, W.; Ghoussoub, M.; Singh, C. V.; Chin, Y.-H. C. Consequences of Surface Oxophilicity of Ni, Ni-Co, and Co Clusters on Methane Activation. *J. Am. Chem. Soc.* **2017**, *139*, 6928−6945.
(61) Yamaguchi, A.; Iglesia, E. Catalytic Activation and Reforming of Methane on Supported Palladium Clusters. *J. Catal.* **2010**, *274*, 52−63.
(62) Wei, J.; Iglesia, E. Mechanism and Site Requirements for Activation and Chemical Conversion of Methane on Supported Pt Clusters and Turnover Rate Comparisons among Noble Metals. *J. Phys. Chem. B* **2004**, *108*, 4094−4103.
(63) Wei, J.; Iglesia, E. Reaction Pathways and Site Requirements for the Activation and Chemical Conversion of Methane on Ru−Based Catalysts. *J. Phys. Chem. B* **2004**, *108*, 7253−7262.
(64) Tsakoumis, N. E.; Rønning, M.; Borg, Ø.; Rytter, E.; Holmen, A. Deactivation of Cobalt Based Fischer−Tropsch Catalysts: A Review. *Catal. Today* **2010**, *154*, 162−182.
(65) Eschemann, T. O.; de Jong, K. P. Deactivation Behavior of Co/TiO_2 Catalysts During Fischer−Tropsch Synthesis. *ACS Catal.* **2015**, *5*, 3181−3188.
(66) Argyle, M. D.; Chen, K.; Bell, A. T.; Iglesia, E. Ethane Oxidative Dehydrogenation Pathways on Vanadium Oxide Catalysts. *J. Phys. Chem. B* **2002**, *106*, 5421−5427.
(67) Annamalai, L.; Liu, Y.; Ezenwa, S.; Dang, Y.; Suib, S. L.; Deshlahra, P. Influence of Tight Confinement on Selective Oxidative Dehydrogenation of Ethane on MoVTeNb Mixed Oxides. *ACS Catal.* **2018**, *8*, 7051−7067.
(68) Dai, G.-L.; Liu, Z.-P.; Wang, W.-N.; Lu, J.; Fan, K.-N. Oxidative Dehydrogenation of Ethane over V_2O_5 (001): A Periodic Density Functional Theory Study. *J. Phys. Chem. C* **2008**, *112*, 3719−3725.
(69) Chen, K.; Xie, S.; Iglesia, E.; Bell, A. T. Structure and Properties of Zirconia-Supported Molybdenum Oxide Catalysts for Oxidative Dehydrogenation of Propane. *J. Catal.* **2000**, *189*, 421−430.
(70) Ji, Z.; Lv, H.; Pan, X.; Bao, X. Enhanced Ethylene Selectivity and Stability of Mo/ZSM5 Upon Modification with Phosphorus in Ethane Dehydrogenation. *J. Catal.* **2018**, *361*, 94−104.
(71) Kwon, S.; Deshlahra, P.; Iglesia, E. Dioxygen Activation Routes in Mars-Van Krevelen Redox Cycles Catalyzed by Metal Oxides. *J. Catal.* **2018**, *364*, 228−247.
(72) Deshlahra, P.; Carr, R. T.; Chai, S.-H.; Iglesia, E. Mechanistic Details and Reactivity Descriptors in Oxidation and Acid Catalysis of Methanol. *ACS Catal.* **2015**, *5*, 666−682.
(73) Chen, X.; Chen, Y.; Song, C.; Ji, P.; Wang, N.; Wang, W.; Cui, L. Recent Advances in Supported Metal Catalysts and Oxide Catalysts for the Reverse Water-Gas Shift Reaction. *Front. Chem.* **2020**, *8*, 709.
(74) Wilson, R. D.; Barton, D. G.; Baertsch, C. D.; Iglesia, E. Reaction and Deactivation Pathways in Xylene Isomerization on Zirconia Modified by Tungsten Oxide. *J. Catal.* **2000**, *194*, 175−187.
(75) Abdelrahman, O. A.; Luo, H. Y.; Heyden, A.; Román-Leshkov, Y.; Bond, J. Q. Toward Rational Design of Stable, Supported Metal Catalysts for Aqueous-Phase Processing: Insights from the Hydrogenation of Levulinic Acid. *J. Catal.* **2015**, *329*, 10−21.

https://doi.org/10.1021/acscatal.2c02525
ACS Catal. 2022, 12, 12227−12245